In compliance with the
Canadian Privacy Legislation
some supporting forms
may have been removed from
this dissertation.

While these forms may be included
in the document page count,
their removal does not represent
any loss of content from the dissertation.

University of Alberta

Photon Propagation Near Rapidly Rotating Neutron Stars

by

Sheldon Scott Campbell

A thesis submitted to the Faculty of Graduate Studies and Research in partial fulfillment of the requirements for the degree of **Master of Science**.

Department of Physics

Edmonton, Alberta
Fall 2003

National Library
of Canada

Acquisitions and
Bibliographic Services

395 Wellington Street
Ottawa ON K1A 0N4
Canada

Bibliothèque nationale
du Canada

Acquisisitons et
services bibliographiques

395, rue Wellington
Ottawa ON K1A 0N4
Canada

Your file Votre référence
ISBN: 0-612-87731-0
Our file Notre référence
ISBN: 0-612-87731-0

The author has granted a non-exclusive licence allowing the National Library of Canada to reproduce, loan, distribute or sell copies of this thesis in microform, paper or electronic formats.

The author retains ownership of the copyright in this thesis. Neither the thesis nor substantial extracts from it may be printed or otherwise reproduced without the author's permission.

L'auteur a accordé une licence non exclusive permettant à la Bibliothèque nationale du Canada de reproduire, prêter, distribuer ou vendre des copies de cette thèse sous la forme de microfiche/film, de reproduction sur papier ou sur format électronique.

L'auteur conserve la propriété du droit d'auteur qui protège cette thèse. Ni la thèse ni des extraits substantiels de celle-ci ne doivent être imprimés ou aturement reproduits sans son autorisation.

Canada

University of Alberta

Library Release Form

Name of Author: Sheldon Scott Campbell

Title of Thesis: Photon Propagation Near Rapidly Rotating Neutron Stars

Degree: Master of Science

Year this Degree Granted: 2003

Permission is hereby granted to the University of Alberta Library to reproduce single copies of this thesis and to lend or sell such copies for private, scholarly or scientific research purposes only.

The author reserves all other publication and other rights in association with the copyright in the thesis, and except as herein before provided, neither the thesis nor any substantial portion thereof may be printed or otherwise reproduced in any material form whatever without the author's prior written permission.

Date: August 22, 2003

University of Alberta

Faculty of Graduate Studies and Research

The undersigned certify that they have read, and recommend to the Faculty of Graduate Studies and Research for acceptance, a thesis entitled **Photon Propagation Near Rapidly Rotating Neutron Stars** submitted by Sheldon Scott Campbell in partial fulfillment of the requirements for the degree of **Master of Science**.

Date: Aug 21, 2003

Abstract

Since the turn of the millennium, spectra of neutron stars have been detected by space-based X-ray telescopes. Since neutron stars are compact, the analysis of their emitted light must take general relativistic effects into account including redshifts, bending of light rays, relativistic Doppler shifts, and frame dragging. In order to include these relativistic effects correctly, ray-tracing simulations must be implemented. The formalism and numerical methods for calculating geodesics and implementing ray-tracing methods within neutron star numerical space-times are presented. As an application for these methods, an approximation of the flux of blackbody emitting neutron stars measured far from the star is calculated. Presented data shows how the flux of the star is affected by its mass, spin, and equation of state.

Twinkle tWinkle *little* Star
how i wonder *what* You are

To my parents for always supporting my goals and believing I will achieve them. And to Melanie, for sharing my dreams and giving me the strength to make them real.

Acknowledgements

I am strongly indebted to Sharon Morsink for introducing me to such a fulfilling project and for showing me how it can be completed, but giving me the freedom to pursue my own solutions. Thank-you Sharon for your countless suggestions on the many versions of this manuscript. I would also like to thank Melanie for running all those programs and helping me compile the data. My gratitude goes out to Don Page for carefully reading this thesis and providing many new insights on the work. This research was partially supported by the Natural Sciences and Engineering Research Council of Canada.

Table of Contents

1 Introduction 1

2 Geodesics about Rapidly Rotating Neutron Stars 5
- 2.1 The Geometry of a Rapidly Rotating Neutron Star 5
- 2.2 Neutron Star Models 7
- 2.3 Massive Test Particles 8
- 2.4 Massless Test Particles 12
- 2.5 Initial Conditions 13
- 2.6 The Poles 15
- 2.7 Numerical Solutions of the Geodesics 16
  - 2.7.1 Embedded Runge-Kutta Pairs 16
  - 2.7.2 Accuracy of the Algorithms 19
  - 2.7.3 Comparison of Runge-Kutta Algorithms 21

3 Neutron Star Emissions 22
- 3.1 Parametrization of the Star's Surface 22
- 3.2 Emission Directions in Curved Space: $D - \dot{\phi}_0$ Parametrization 23
- 3.3 Altitude-Azimuth Coordinate System in Flat Space 26
- 3.4 Altitude-Azimuth Coordinate System in Curved Space 27
  - 3.4.1 A Spacelike 3-Metric for a Neutron Star 27
  - 3.4.2 Altitudes from a Neutron Star Surface 28
  - 3.4.3 Azimuth Angles on the Neutron Star Horizon 29
  - 3.4.4 Discretization of the Altitude-Azimuth System 35
  - 3.4.5 Summary of the Altitude-Azimuth System 37
- 3.5 Initial Surface Position and Geodesic Accuracy 38
  - 3.5.1 Accuracy Measured With ε^* 38
  - 3.5.2 Accuracy of Geodesics from Spherical Stars 39
  - 3.5.3 Accuracy of Geodesics in the Equatorial Plane of Rotating Stars 40
  - 3.5.4 Deflection of Geodesics in the Equatorial Plane 41

4 The Thermal Flux from Rapidly Rotating Neutron Stars **45**
4.1 Introduction 45
4.2 Solid Angles in Curved Space 46
4.3 Specific Intensity and Photon Number 47
4.4 The Flux from a Neutron Star Received by a Telescope Far from the Star 48
4.5 The Flux Received from a Spherical Neutron Star 52
4.5.1 The Spherical Limit of the Calculated Flux 52
4.5.2 The Exact Flux of a Spherical Star 60
4.6 Calculating the Flux: Results 62

5 Conclusions **69**
5.1 Summary of Completed Research 69
5.2 Computational Improvements Required 70
5.3 Future Directions for Research 71

List of Figures

2.1 The modified Butcher table. It specifies an explicit formula for an embedded Runge-Kutta pair RK$p(q)$ used to approximate an autonomous set of differential equations. 18

2.2 Embedded Runge-Kutta pairs. 19

2.3 Plot of ε_n^* vs. λ_n for the three RK implementations. The plot actually continues until $\lambda \approx 205$, but ε_n^* remains less than 10^{-8} for $\lambda > 20$. The tolerances used were $T = 10^{-(p+4)}$ where p is the order of the algorithm. The star in this example has equation of state eos L, mass $M = 1.4M_\odot$, and frequency $f = 600$ Hz. The initial conditions of the geodesic are $s_0 = 0.5$, $\mu_0 = 0.5$, $\phi_0 = 0$, $\dot{r}_0 = 0.4$, $\dot{\mu}_0 = 0.1$, and $\dot{\phi}_s = +1$. 20

2.4 Some statistics for the algorithms specified in figure 2.2 calculated for the geodesic described in figure 2.3. 21

3.1 The points considered on the surface of a neutron star are separated by a small polar angle $\Delta\theta$. This picture shows an example where $\theta_{N_\theta} > 0$. 23

3.2 Parametrizing the directions away from a point of the surface with D. 24

3.3 The altitude-azimuth $(h - A)$ coordinate system. Also shown in this diagram is the zenith angle z, hemisphere radius δ, and cylindrical radius ρ. (Figure adapted from Carroll and Ostlie [8]). 26

3.4 A plot of the maximum value of ε^* for each position on the star's surface vs. θ for 3 stars. The stars have equation of state eos L, mass $M = 1.4M_\odot$, and varying frequencies. This plot reveals a number of pathological cases resulting in less accuracy for some geodesics. 39

3.5 Same as in figure 3.4 except that the 3rd highest value of ε^* is plotted for each position on the star's surface. The lack of pathological cases illustrates how few they are compared to the total number of calculated geodesics. 40

3.6 Maximum values of error estimators for non-rotating stars. The star in this calculation had equation of state eos L, mass $M = 1.4M_\odot$. 41

3.7 Error estimators for rotating stars. The star in this calculation had equation of state eos L, mass $M = 1.4M_\odot$, and frequency 600 Hz. 42
3.8 The maximum angular displacement of prograde and retrograde photons confined in the equatorial plane of stars with eos A, rotating at various frequencies. 43
3.9 The maximum angular displacement of photons confined in the equatorial plane of stars with eos APR. 43
3.10 The maximum angular displacement of photons confined in the equatorial plane of stars with eos L. 44

4.1 In curved space-time, the value of a solid angle is different at different distances from the origin due to lensing effects. The surface of the light cone is generated by geodesics. 45
4.2 A solid angle $d\Omega$. In Cartesian space, the solid angle subtended by dA_Ω is equal to the solid angle subtended by dA'_Ω at O. . . 46
4.3 Emission of radiation. 47
4.4 The radiation emitted from a star rotating with angular velocity Ω. The radiation is emitted from dA at an altitude h from the surface so that it reaches the telescope with area dA' far from the star. 49
4.5 A plot of $f(u) = (1-2u)u^2$. 55
4.6 The roots of $u_b^2 - (1-2u)u^2$. 56
4.7 The fractional difference between $\mathcal{F}_{\text{sph}}$ and $\mathcal{F}^*_{\text{sph}}$ increases as $\frac{M}{R}$ increases. 61
4.8 Constructed functions $\sin h(\phi)$ for various initial latitudes on a spherical star of mass $M = 1.4M_\odot$ and equation of state A where the observer is located in the star's equatorial plane. The points are the calculated values of the function from the emission of the neutron star, and the lines cover the theoretical values determined from solving (4.33) and (4.29) for h given the appropriate angular displacement φ. The curves cross at $\phi_0 = \frac{\pi}{2}$ where they take the value of the altitude of the photon reaching the observer from the star's poles. 63
4.9 This figure represents the star's sky. The points are final destinations of a set of photons all propagating with the same altitude from one position on the star's surface. The horizontal lines represent lines of constant latitude in the star's sky. It is expected that the photons should follow a pattern similar to the left diagram where each latitude has at most two geodesics reach it. The right diagram contains an example of a "blip" where one of the points is misplaced due to numerical error in such a way that an interval of latitudes (shown by the vertical arrow) have more than two geodesics reach it. 64

4.10 The fractional difference between $\mathcal{F}$ and $\mathcal{F}_{\text{sph}}$ for all calculated spherical models where $\mathcal{F}$ is calculated with the observer in the star's equatorial plane. 65
4.11 The fractional difference between ϕ_{max} and φ_{max} for the calculated spherical neutron star models. 65
4.12 The calculated flux from a non-rotating star of eos A and mass $1.4M_{\odot}$ for observers at various latitudes. The constant line is $\mathcal{F}_{\text{sph}}$, the expected spherical limit of the flux. 66
4.13 The flux from a star with eos A and mass $1.4M_{\odot}$ rotating with a frequency of 600 Hz for observers at different latitudes as calculated by our algorithms. This figure is meant as an indication of the current shortcomings of the code. As with figure 4.12, the vanishing of the flux at the pole is a non-physical numerical artifact. The plot should be most accurate for observers near the equator. 66
4.14 The fractional increase in measured flux by an observer in the neutron star's equatorial plane as the star's spin frequency increases. 67
4.15 The fractional increase in measured flux per surface area of neutron stars as their spin frequencies increase. 68

Chapter 1

Introduction

A neutron star is the end product in the evolution of a large star; the cold remains of what was once a bright beacon. Stars with large enough masses ($M \gtrsim 8M_{\odot}$ during the main sequence phase) develop an iron core which is unstable to gravitational collapse. These cores, typically $1.5M_{\odot}$, are heavier than the Chandrasekhar Mass and are unable to be supported by electron degeneracy pressure. During collapse, the core's density increases to where reverse beta decay occurs: a proton and electron join to produce a neutron and release a neutrino [30]. The neutrons collapse until they become degenerate, at which point neutron degeneracy pressure halts their collapse, forming a neutron star. The collision of the outer infalling layers of the dying star with the hard surface of the neutron star triggers a type II supernova.

The radius of the neutron star is of the order of 10–15 km. Angular momentum conservation leads to a decrease in the core's period by about 6 orders of magnitude during its collapse [8]. Young neutron stars have been observed to rotate with frequencies of 30–40 Hz, but neutron stars can be spun up to faster rotation rates by accreting matter from companion stars in binary systems and have been observed rotating with frequencies as high as 650 Hz [16]. Magnetic fields are also magnified during the core's collapse as magnetic field lines are compressed together. Internal fields of 10^5 G prior to collapse will increase to fields of $\sim 10^{15}$ G in the resulting neutron star [8].

With a thermal flux of a neutron star 5 kpc away detected to be on the order of 10^{-12} erg cm^{-2} s^{-1} [28]. neutron stars are one of the dimmest fundamental

solar-mass astrophysical objects known to astronomers, brighter only than black holes. Knowledge of their existence is owed to their relativistic natures: intense pulsar emissions from rotating neutron stars have been recorded from radio to gamma wavelengths, and neutron stars in binary systems that accrete matter from their companion give off bright X-ray bursts. We continue to learn about neutron stars from observations of these phenomena.

Still, there remains much to be understood about the dense exotic matter that makes up neutron stars. The density at the core of the neutron star is of the order of 10^{15} g/cm^3, 10 times greater than the typical density of an atomic nucleus. Such densities are beyond what can currently be created in the lab, and so our experimental knowledge of this material is limited to what can be deduced from observing neutron stars. Although observations have provided numerous constraints on the equation of state, many uncertainties still exist. Current models of neutron stars are strongly dependent on the stellar material's equation of state.

With the increased sensitivity of telescopes, especially X-ray telescopes, astronomers are now able to make more detailed measurements of emissions from neutron stars due to pulsar signals and X-ray bursts. Recently, the European Space Agency's XMM X-ray telescope detected spectral lines from within an X-ray burst believed to have originated from the surface of the neutron star [11]. The redshift and spread of these spectral lines contain important information about the mass, distance, and rotation of the neutron star.

As I already alluded to, telescopes are also now able to detect thermal emissions from neutron stars. NASA's Chandra X-ray telescope has recorded the thermal spectrum of several neutron stars [18]. Because neutron stars are relativistic objects, there are several effects that must be taken into account when analyzing the radiation they emit. I already mentioned the well-understood gravitational redshift. The curvature of light rays near the neutron star can allow a significant portion of the rear of the star to be visible to an observer. If the star is rotating, relativistic Doppler shifts can be large, resulting in the spreading of a spectrum: light emitted from portions of the star rotating to-

ward the observer are blue-shifted, and emissions from the star's retreating side are red-shifted. There are also frame-dragging effects that deflect photons (even those with zero angular momentum) in the direction of the star's rotation.

It becomes clear that in order to discuss the flux or spectrum of radiation emitted from the surface of a neutron star, it is important to keep track of the point of origin on the star's surface of each photon that reaches the observer in order to correctly the determine the red (blue)-shift of each photon. This requires ray-tracing methods. A large body of literature [19, 26, 15, 21, 5] already addresses the propagation of light emitted by a spherical relativistic star. This problem is relatively simple since the orbits can be solved by quadrature. Some progress has also been made on the problem of light emitted by a region close to a rotating black hole [27, 6], which is also solvable by quadrature. However, a rapidly rotating neutron star is not well described by either a spherical solution or by a rotating black hole solution. Attempts to calculate rotational effects by perturbatively applying Doppler shifts to the spherical solution [23] still don't consider effects such as frame-dragging. Instead, the rotating neutron star's geometry must be solved numerically [14, 10], and the numerical integration of the photon geodesics performed for each photon emitted.

The object of this research is to provide a computational approach for analyzing thermal emissions from neutron stars so that they may be used to extract useful information about the stars from which they originated.

Chapter 2 describes how to solve for the paths of photons in the neighborhood of a neutron star. Section 2.1 provides a brief review of the geometry of a neutron star. Section 2.3 calculates the equations of motion of massive particles near a neutron star, which is useful for determining the equations of motion of massless particles as shown in section 2.4. Initial conditions for the equations are discussed in 2.5. Because the equations of motion are derived in spherical coordinates, it is inevitable that they are ill behaved at the poles ($\theta = 0, \pi$). These difficulties are discussed in 2.6. The numerical method for solving the equations is presented in 2.7.

In chapter 3, the problem of parametrizing the emission of photons from

the surface of a neutron star is considered. A mathematical description of the neutron star's surface is introduced in 3.1. Section 3.2 describes a coordinate system useful for describing directions away from the neutron's star surface that is easily obtained in the neutron star's geometry. The altitude-azimuth coordinate system is a very natural way for describing angles from a position on the surface of the star. This system is reviewed in 3.3 and derived for the geometry of the neutron star in 3.4. Once we have a framework for calculating emissions from neutron stars, 3.5 discusses the accuracy of the calculated geodesics and its relation to the geodesics' origins on the star's surface.

As an application of this work, chapter 4 contains the calculations of thermal flux detected from a neutron star by an observer far from the star and describes how these observations could be used to determine the radius of the star. The derivation of the flux is presented in 4.2–4.5 and the results of the calculations are in 4.6. Although most general relativistic effects are accounted for, geodesic deviation is neglected. The consequences of this simplification are also considered.

A conclusion and discussion of future directions for this research are provided in chapter 5.

Chapter 2

Geodesics about Rapidly Rotating Neutron Stars

2.1 The Geometry of a Rapidly Rotating Neutron Star

In our discussion, we consider a solitary neutron star centered at the origin of a spherical coordinate system (r, θ, ϕ) rotating in the ϕ direction.

The metric for a rotating neutron star rotating uniformly with angular velocity Ω as measured by an observer at infinity can be expressed in the form [13]

$$\begin{aligned} ds^2 &= g_{ab}dx^a dx^b \\ &= -e^{\gamma+\rho}dt^2 + e^{2\alpha}\left(dr^2 + r^2 d\theta^2\right) + e^{\gamma-\rho}r^2\sin^2\theta(d\phi - \omega dt)^2 \qquad (2.1) \\ &= -e^{\gamma+\rho}dt^2 + e^{2\alpha}\left(dr^2 + \frac{r^2}{1-\mu^2}d\mu^2\right) + e^{\gamma-\rho}r^2(1-\mu^2)(d\phi - \omega dt)^2 \end{aligned}$$

where it becomes increasingly convenient through this discussion to use $\mu = \cos\theta$, and the metric potentials γ, ρ, α, and ω are functions of r and μ only, since we assume a stationary axisymmetric spacetime. In this definition, $\theta = 0$ at the north pole and $\theta = \frac{\pi}{2}$ at the equator.

In the Newtonian limit, $\frac{1}{2}(\gamma + \rho) - 1$ is interpreted as the Newtonian gravitational potential. The circumference of a circle centered about the rotation axis is

$$C = 2\pi r \sin\theta e^{(\gamma-\rho)/2}. \qquad (2.2)$$

In the limit of non-rotating neutron stars, the potentials take the form

$$\lim_{\Omega\to 0} e^{(\gamma-\rho)/2} = \lim_{\Omega\to 0} e^{\alpha} = \left(1+\frac{M}{2r}\right)^2 \tag{2.3}$$

$$\lim_{\Omega\to 0} e^{(\gamma+\rho)/2} = \frac{1-\frac{M}{2r}}{1+\frac{M}{2r}} \tag{2.4}$$

$$\lim_{\Omega\to 0} \omega = \Omega \tag{2.5}$$

outside the star. Here, M is the gravitational mass of the star. In this limit, the metric is simply the Schwarzschild metric in isotropic form [29]. So r corresponds to the isotropic radial coordinate in this limit.

A neutron star's matter can be modeled by a perfect fluid and therefore has a stress-energy tensor given by

$$T^{ab} = (\epsilon + p)u^a u^b + p g^{ab} \tag{2.6}$$

where ϵ is the energy density, p is the pressure, and u^a is the 4-velocity of the fluid, given by

$$u^a = u^t(t^a + \Omega\phi^a) \tag{2.7}$$

$$u^t = \frac{e^{-(\gamma+\rho)/2}}{\sqrt{1-v_\Omega^2}} \tag{2.8}$$

$$v_\Omega = e^{-\rho}(\Omega-\omega)r\sqrt{1-\mu^2}. \tag{2.9}$$

Here, the Killing vectors t^a and ϕ^a satisfy

$$t^a\nabla_a t = \phi^a\nabla_a\phi = 1,$$
$$t^a\nabla_a\phi = \phi^a\nabla_a t = 0.$$

We can numerically solve for the metric potentials of a star with a specified energy density at the center of the star, ϵ_c, and ratio of equatorial radius to polar radius, $\frac{r_e}{r_p}$. This is done by solving Einstein's equations using the Komatsu-Eriguchi-Hachisu method [17]. This involves writing Einstein's equations in integral form using Green's functions and using them to iteratively solve for the potentials. The software used to carry out this calculation was written by Nikolaos Stergioulas [32].

When calculating the potentials, there are inherent difficulties in calculating their dependence on the radial coordinate r since it reaches to infinity. This problem is alleviated by introducing the radial coordinate [10]

$$s = \frac{r}{r + r_e} \tag{2.10}$$

where r_e is the equatorial radius of the star. Then $0 \leq s < 1$ and $s = \frac{1}{2}$ on the star's equator. The potentials are then calculated as functions of s and μ.

In our implementation, we choose an upper limit for s, typically 0.9999. The neutron star space-times I used in my calculations used a grid spacing of 301 values in the s-interval from 0 to 0.9999, and 151 points for μ from 0 to 1. Calculation of the space-time of one rotating star uses about 6 MB of RAM and takes 3 seconds of CPU time on an athlon AMD 1900+ processor with RedHat 7.3 operating system.

2.2 Neutron Star Models

In the introduction, I mentioned that neutron star models are dependent on the uncertain equation of state of the neutron star material. Among other things, the equation of state affects the mass-radius relation, and the upper limits on mass and rotation of neutron stars. Theorists have applied many ideas from nearly every fundamental branch of physics to calculate potential equations of state and a great variety exist that are consistent with current observations [10].

Soft equations of state result in stars with smaller radii, while stars with stiff equations of state have larger radii. Neutron stars with more mass have smaller radii, so that the most compact (and hence most relativistic) stars are the most massive.

Since there is still a great deal of uncertainty in the equation of state of neutron star matter, we have chosen three representative equations of state spanning the allowed range of stiffness. We have chosen two older equations of state from the Arnett and Bowers 1977 catalogue [3], labeled eos A and eos L, as well as a more recent equation of state labeled eos APR. The softest

equation of state is eos A, eos L is the stiffest, and eos APR has intermediate stiffness.

The maximum mass of a non-rotating neutron star with eos A is 1.65 $M_\odot$ with a corresponding minimum radius of 8.5 km. The maximum frequency of rotation of a star with the maximum mass is about 1400 Hz. The radius of a non-rotating star with a mass of 1.4 $M_\odot$ (the Chandrasekhar mass) and eos A is 10 km, and the maximum rotation frequency for the star of that mass is about 1300 Hz [24, 10]. This equation of state is on the edge of what is allowed from observations. Vela X1 has an observed mass of $M \geq (1.78 \pm 0.15) M_\odot$ [4], and Cygnus X2 has a mass of $M = (1.78 \pm 0.23) M_\odot$ [22].

Spherical neutron stars with eos L have a maximum mass of 2.7 $M_\odot$ and a corresponding radius of 13.5 km. Stars of this mass have a maximum rotation frequency of 1000 Hz. Neutron stars with mass 1.4 $M_\odot$ have a radius of 15 km when non-rotating, and can rotate up to a frequency of 700 Hz [25, 10].

An example of an equation of state somewhere between the stiffness extremes of eos A and eos L, eos APR is described in [1] labeled there as A18+δv+UIX*. Its most massive spherical star is 2.2 $M_\odot$ with a radius of 10 km. A 2.2 $M_\odot$ star has a maximum frequency of rotation of 1400 Hz. Stars of 1.4 $M_\odot$ have a maximum rotation frequency of about 1000 Hz and have a radius of 11.5 km when they are not rotating.

2.3 Massive Test Particles

Because the metric is independent of t and ϕ, t^a and ϕ^a are Killing vectors of the space-time. So a free particle in the space-time has the conserved momentum components [20]

$$p_t = -E, \quad p_\phi = L_z \tag{2.11}$$

where E is the energy of the particle and L_z is the z-component of its angular momentum.

Consider a test particle of mass m freely traveling in the space-time of a neutron star with energy E and z-angular momentum L_z. The 4-momentum

of the particle is

$$\begin{aligned} p_a &= mu_a \\ &= -E\nabla_a t + L_z\nabla_a\phi + e^{2\alpha}m\left(\frac{dr}{d\tau}\nabla_a r + \frac{r^2}{1-\mu^2}\frac{d\mu}{d\tau}\nabla_a\mu\right) \end{aligned} \tag{2.12}$$

where τ is the proper time. Using the kinematic definition of momentum, we have

$$\begin{aligned} \frac{dt}{d\tau} &= \frac{p^t}{m} = \frac{1}{m}(g^{tt}p_t + g^{t\phi}p_\phi) \\ &= e^{-(\gamma+\rho)}\frac{E-\omega L_z}{m}, \end{aligned} \tag{2.13}$$

$$\begin{aligned} \frac{d\phi}{d\tau} &= \frac{p^\phi}{m} = \frac{1}{m}(g^{\phi t}p_t + g^{\phi\phi}p_\phi) \\ &= \omega e^{-(\gamma+\rho)}\frac{E-\omega L_z}{m} + e^{\rho-\gamma}\frac{L_z}{mr^2(1-\mu^2)}. \end{aligned} \tag{2.14}$$

Momentum conservation $p_a p^a = -m^2$ results in

$$\left(\frac{dr}{d\tau}\right)^2 + \frac{r^2}{1-\mu^2}\left(\frac{d\mu}{d\tau}\right)^2 = \frac{E^2}{m^2}\mathcal{P} - e^{-2\alpha} \tag{2.15}$$

where I define

$$\mathcal{P} \equiv e^{-2\alpha}\mathcal{Q}, \tag{2.16}$$

$$\mathcal{Q} \equiv e^{-\gamma}\left[e^{-\rho}\left(1-\frac{\omega L_z}{E}\right)^2 - e^{\rho}\frac{L_z^2}{E^2r^2(1-\mu^2)}\right]. \tag{2.17}$$

The equations for the r and μ coordinates of the particle are determined from the geodesic equations [20, 29, 33]

$$\frac{d^2x^a}{d\tau^2} + \Gamma^a_{bc}\frac{dx^b}{d\tau}\frac{dx^c}{d\tau} = 0 \tag{2.18}$$

where

$$\Gamma^a_{bc} = \frac{1}{2}g^{ad}(g_{bd,c} + g_{cd,b} - g_{bc,d}) \tag{2.19}$$

are the Christoffel symbols. Note that the comma represents partial differentiation. Evaluating (2.18) for each coordinate gives:

$$\begin{aligned} \frac{d^2t}{d\tau^2} &+ (\gamma_{,r} + \rho_{,r} - e^{-2\rho}\omega_{,r}\omega r^2(1-\mu^2))\frac{dt}{d\tau}\frac{dr}{d\tau} \\ &+ (\gamma_{,\mu} + \rho_{,\mu} - e^{-2\rho}\omega_{,\mu}\omega r^2(1-\mu^2))\frac{dt}{d\tau}\frac{d\mu}{d\tau} \\ &+ e^{-2\rho}\omega_{,r}r^2(1-\mu^2)\frac{d\phi}{d\tau}\frac{dr}{d\tau} + e^{-2\rho}\omega_{,\mu}r^2(1-\mu^2)\frac{d\phi}{d\tau}\frac{d\mu}{d\tau} = 0 \end{aligned} \tag{2.20}$$

$$\frac{d^2\phi}{d\tau^2} + 2\omega\left\{\left[\rho_{,r} - \frac{1}{r} - \frac{\omega_{,r}}{2\omega} - \frac{1}{2}e^{-2\rho}\omega_{,r}\omega r^2(1-\mu^2)\right]\frac{dt}{d\tau}\frac{dr}{d\tau}\right.$$
$$+ \left.\left[\rho_{,\mu} + \frac{\mu}{1-\mu^2} - \frac{\omega_{,\mu}}{2\omega} - \frac{1}{2}e^{-2\rho}\omega_{,\mu}\omega r^2(1-\mu^2)\right]\frac{dt}{d\tau}\frac{d\mu}{d\tau}\right\}$$
$$+ \left(\gamma_{,r} - \rho_{,r} + \frac{2}{r} + e^{-2\rho}\omega_{,r}\omega r^2(1-\mu^2)\right)\frac{d\phi}{d\tau}\frac{dr}{d\tau}$$
$$+ \left(\gamma_{,\mu} - \rho_{,\mu} - \frac{2\mu}{1-\mu^2} + e^{-2\rho}\omega_{,\mu}\omega r^2(1-\mu^2)\right)\frac{d\phi}{d\tau}\frac{d\mu}{d\tau} = 0 \quad (2.21)$$

$$\frac{d^2r}{d\tau^2} + e^{\gamma-\rho-2\alpha}\left\{\left[\frac{1}{2}e^{2\rho}(\gamma_{,r} + \rho_{,r})\right.\right.$$
$$- \left.\omega^2r^2(1-\mu^2)\left(\frac{\gamma_{,r} - \rho_{,r}}{2} + \frac{\omega_{,r}}{\omega} + \frac{1}{r}\right)\right]\left(\frac{dt}{d\tau}\right)^2$$
$$+ 2\omega r^2(1-\mu^2)\left(\frac{\gamma_{,r} - \rho_{,r}}{2} + \frac{\omega_{,r}}{2\omega} + \frac{1}{r}\right)\frac{dt}{d\tau}\frac{d\phi}{d\tau}$$
$$- \left.r^2(1-\mu^2)\left(\frac{\gamma_{,r} - \rho_{,r}}{2} + \frac{1}{r}\right)\left(\frac{d\phi}{d\tau}\right)^2\right\}$$
$$+ \alpha_{,r}\left(\frac{dr}{d\tau}\right)^2 + 2\alpha_{,\mu}\frac{dr}{d\tau}\frac{d\mu}{d\tau} - \frac{r^2}{1-\mu^2}\left(\alpha_{,r} + \frac{1}{r}\right)\left(\frac{d\mu}{d\tau}\right)^2 = 0 \quad (2.22)$$

$$\frac{d^2\mu}{d\tau^2} + \frac{1-\mu^2}{r^2}e^{\gamma-\rho-2\alpha}\left\{\left[\frac{1}{2}e^{2\rho}(\gamma_{,\mu} + \rho_{,\mu})\right.\right.$$
$$- \left.\omega^2r^2(1-\mu^2)\left(\frac{\gamma_{,\mu} - \rho_{,\mu}}{2} + \frac{\omega_{,\mu}}{\omega} - \frac{\mu}{1-\mu^2}\right)\right]\left(\frac{dt}{d\tau}\right)^2$$
$$+ 2\omega r^2(1-\mu^2)\left(\frac{\gamma_{,\mu} - \rho_{,\mu}}{2} + \frac{\omega_{,\mu}}{2\omega} - \frac{\mu}{1-\mu^2}\right)\frac{dt}{d\tau}\frac{d\phi}{d\tau}$$
$$- \left.r^2(1-\mu^2)\left(\frac{\gamma_{,\mu} - \rho_{,\mu}}{2} - \frac{\mu}{1-\mu^2}\right)\left(\frac{d\phi}{d\tau}\right)^2\right\} - \frac{1-\mu^2}{r^2}\alpha_{,\mu}\left(\frac{dr}{d\tau}\right)^2$$
$$+ 2\left(\alpha_{,r} + \frac{1}{r}\right)\frac{dr}{d\tau}\frac{d\mu}{d\tau} + \left(\alpha_{,\mu} + \frac{\mu}{1-\mu^2}\right)\left(\frac{d\mu}{d\tau}\right)^2 = 0. \quad (2.23)$$

I include the equations for t and ϕ only for completeness. Simple substitution shows that (2.20) and (2.21) are satisfied by (2.13) and (2.14). This is expected since the existence of the two constants of motion E and L_z has the consequence that geodesic equations for $\frac{d^2t}{d\tau^2}$ and $\frac{d^2\phi}{d\tau^2}$ carry no new information.

Using (2.13)–(2.15) in (2.22) and (2.23) gives us the equations of motion

for r and μ:

$$\frac{d^2r}{d\tau^2} = \frac{E^2}{m^2}\left[\left(\alpha_{,r}+\frac{1}{r}\right)\mathcal{P}-\mathcal{R}\right]-\left(2\alpha_{,r}+\frac{1}{r}\right)\left(\frac{dr}{d\tau}\right)^2 - 2\alpha_{,\mu}\frac{dr}{d\tau}\frac{d\mu}{d\tau} \tag{2.24}$$

$$\frac{d^2\mu}{d\tau^2} = \frac{E^2}{m^2}\frac{1-\mu^2}{r^2}\left(\alpha_{,\mu}\mathcal{P}-\mathcal{M}\right)-\left(2\alpha_{,\mu}+\frac{\mu}{1-\mu^2}\right)\left(\frac{d\mu}{d\tau}\right)^2 - 2\left(\alpha_{,r}+\frac{1}{r}\right)\frac{dr}{d\tau}\frac{d\mu}{d\tau} \tag{2.25}$$

where

$$\mathcal{R} \equiv -\frac{1}{2}e^{-2\alpha}\frac{\partial\mathcal{Q}}{\partial r} \tag{2.26}$$

$$= e^{-2\alpha}\left\{e^{-(\gamma+\rho)}\left(1-\frac{\omega L_z}{E}\right)\left[\left(1-\frac{\omega L_z}{E}\right)\frac{\gamma_{,r}+\rho_{,r}}{2}+\frac{\omega_{,r}L_z}{E}\right] - e^{\rho-\gamma}\left(\gamma_{,r}-\rho_{,r}+\frac{1}{r}\right)\frac{L_z^2}{E^2r^2(1-\mu^2)}\right\}$$

$$\mathcal{M} \equiv -\frac{1}{2}e^{-2\alpha}\frac{\partial\mathcal{Q}}{\partial\mu} \tag{2.27}$$

$$= e^{-2\alpha}\left\{e^{-(\gamma+\rho)}\left(1-\frac{\omega L_z}{E}\right)\left[\left(1-\frac{\omega L_z}{E}\right)\frac{\gamma_{,\mu}+\rho_{,\mu}}{2}+\frac{\omega_{,\mu}L_z}{E}\right] - e^{\rho-\gamma}\left(\gamma_{,\mu}-\rho_{,\mu}-\frac{\mu}{1-\mu^2}\right)\frac{L_z^2}{E^2r^2(1-\mu^2)}\right\}.$$

Equations (2.13),(2.14),(2.15),(2.24), and (2.25) correspond to the set of equations determining the time evolution of an orbit. This set contains one too many equations; however, we can use equation (2.15) as a check on the accuracy of our code that solves the equations.

A major difference between the geodesic equations for rotating neutron stars and black holes exists. A third constant of motion, known as the Carter constant [9] exists for the Kerr solution describing a rotating black hole. The existence of the Carter constant allows the geodesic equations to be written as only first derivatives of the coordinates in such a way that the solution can be written as elliptic integrals. No analogous constant exists for motion near a rotating neutron star, so the solution of the geodesic equations is more difficult.

2.4 Massless Test Particles

When considering orbits of massless particles, we can no longer parametrize the orbits with respect to the proper time τ since proper time vanishes for massless particles. Instead, it is convenient to parametrize with respect to the affine parameter

$$\lambda = \lim_{m \to 0} \frac{E}{m} \tau. \tag{2.28}$$

Instead of requiring two independent parameters E and L_z, the resulting equations require only the single parameter

$$b = \frac{L_z}{E} \tag{2.29}$$

called the *impact parameter*. Making these substitutions into the equations of the last section, we get the equations of motion for photons to be:

$$\frac{dt}{d\lambda} = e^{-(\gamma+\rho)}(1 - \omega b) \tag{2.30}$$

$$\frac{d\phi}{d\lambda} = \omega e^{-(\gamma+\rho)}(1 - \omega b) + e^{\rho-\gamma}\frac{b}{r^2(1-\mu^2)} \tag{2.31}$$

$$\frac{dr}{d\lambda} = \dot{r} \tag{2.32}$$

$$\frac{d\mu}{d\lambda} = \dot{\mu} \tag{2.33}$$

$$\frac{d\dot{r}}{d\lambda} = \left(\alpha_{,r} + \frac{1}{r}\right)\mathcal{P} - \mathcal{R} - \left(2\alpha_{,r} + \frac{1}{r}\right)\dot{r}^2 - 2\alpha_{,\mu}\dot{r}\dot{\mu} \tag{2.34}$$

$$\frac{d\dot{\mu}}{d\lambda} = \frac{1-\mu^2}{r^2}(\alpha_{,\mu}\mathcal{P} - \mathcal{M}) - \left(2\alpha_{,\mu} + \frac{\mu}{1-\mu^2}\right)\dot{\mu}^2 - 2\left(\alpha_{,r} + \frac{1}{r}\right)\dot{r}\dot{\mu} \tag{2.35}$$

$$\mathcal{P} = e^{-2\alpha}\mathcal{Q} \tag{2.36}$$

$$\mathcal{R} = -\frac{1}{2}e^{-2\alpha}\frac{\partial \mathcal{Q}}{\partial r} \tag{2.37}$$

$$\mathcal{M} = -\frac{1}{2}e^{-2\alpha}\frac{\partial \mathcal{Q}}{\partial \mu} \tag{2.38}$$

$$\mathcal{Q} = e^{-(\gamma+\rho)}(1 - \omega b)^2 - e^{\rho-\gamma}\frac{b^2}{r^2(1-\mu^2)} \tag{2.39}$$

with the momentum conservation constraint

$$\dot{r}^2 + \frac{r^2}{1-\mu^2}\dot{\mu}^2 = \mathcal{P}. \tag{2.40}$$

Because of the astronomical lengths involved, it is not practical to numerically calculate solutions of these equations in cgs units. Instead, dimensionless

variables are defined by introducing a length scale:

$$\begin{aligned} \bar{r} &= \frac{r}{\sqrt{\kappa}} \\ \bar{\lambda} &= \frac{\lambda}{\sqrt{\kappa}} \end{aligned}$$

where the length scale squared is given by [10]

$$\kappa \equiv \frac{c^2}{G\epsilon_o} \tag{2.41}$$

with c being the speed of light, G the universal gravitational constant, and $\epsilon_o = 10^{15}\text{g/cm}^3$. This length scale can also be used to create dimensionless energies, densities, pressures, etc.

Because the metric potentials are calculated as functions of s and μ, the implemented equations calculate the photon paths explicitly with the coordinate s given in (2.10) instead of r.

2.5 Initial Conditions

We require sufficient initial conditions in order to solve the photon equations of motion. This section describes one convenient set of initial conditions.

First needed is the initial position of the geodesic: $t(0) \equiv t_0$, $r(0) \equiv r_0$, $\mu(0) \equiv \mu_0$, and $\phi(0) \equiv \phi_0$. This gives us initial values of the metric potentials denoted by $\alpha(r_0, \mu_0) \equiv \alpha_0$, etc. It is clear from the equations that we also require the initial r and μ velocities of the photon: $\frac{dr}{d\lambda}\big|_{\lambda=0} \equiv \dot{r}_0$ and $\frac{d\mu}{d\lambda}\big|_{\lambda=0} \equiv \dot{\mu}_0$. These initial conditions do not yet specify a unique geodesic, but in general allow for two geodesics: one co-rotating with the star, and the other counter-rotating. To specify a preference, we must also give the sign of the initial phi velocity, given by

$$\dot{\phi}_s \equiv \text{sign}(\dot{\phi}_0) = \begin{cases} 1 \text{ when } \dot{\phi}_0 > 0 \\ -1 \text{ when } \dot{\phi}_0 < 0 \end{cases} . \tag{2.42}$$

From these initial conditions we can determine the initial values of the right-hand-sides of the equations (2.30)–(2.35) once we determine the value of b. This can be found from the initial conditions by rearranging (2.40) to solve

for b. This gives

$$b = d_0 \frac{-v_0 + \kappa_s \sqrt{1 - q_0^2(1 - v_0^2)}}{1 - v_0^2} \tag{2.43}$$

where

$$\kappa_s = \pm 1, \tag{2.44}$$

$$d_0 = e^{-\rho_0} r_0 \sqrt{1 - \mu_0^2}, \tag{2.45}$$

$$v_0 = \omega_0 d_0 \tag{2.46}$$

$$q_0 = e^{\alpha_0 + (\gamma_0 + \rho_0)/2} \sqrt{\dot{r}_0^2 + \frac{r_0^2}{1 - \mu_0^2} \dot{\mu}_0^2}. \tag{2.47}$$

To determine the correct sign, substitute (2.43) into (2.31).

$$\begin{aligned} \left.\frac{d\phi}{d\lambda}\right|_{\lambda=0} &= e^{-(\gamma_0+\rho_0)} \left(\omega_0 + \frac{1 - v_0^2}{d_0^2} b \right) \\ &= e^{-(\gamma_0+\rho_0)} \left(\omega_0 + \frac{-v_0 + \kappa_s \sqrt{1 - q_0^2(1 - v_0^2)}}{d_0} \right) \\ &= \kappa_s \underbrace{e^{-(\gamma_0+\rho_0)} \frac{\sqrt{1 - q_0^2(1 - v_0^2)}}{d_0}}_{\geq 0} \end{aligned}$$

This shows that $\kappa_s = \dot{\phi}_s$. One may wonder what the value of κ_s needs to be when $\dot{\phi}_0 = 0$. It turns out that in this case we have $1 - q_0^2(1 - v_0^2) = 0$ and so the value of κ_s does not affect the value of b. To see this result, assume $\dot{\phi}_0 = 0$. Then (2.31) tells us that

$$b = \frac{d_0 v_0}{v_0^2 - 1}.$$

Using this with (2.47) and (2.40) gives

$$\begin{aligned} q_0^2 &= e^{2\alpha_0 + \gamma_0 + \rho_0} \mathcal{P}_0 \\ &= (1 - \omega_0 b)^2 - \frac{b^2}{d_0^2} \\ &= \left(1 + \frac{v_0^2}{1 - v_0^2} \right)^2 - \frac{1}{d_0^2} \left(\frac{d_0 v_0}{1 - v_0^2} \right)^2 \\ &= \frac{1}{1 - v_0^2} \end{aligned}$$

$$\implies 0 = 1 - q_0^2(1 - v_0^2) \qquad (\dot{\phi}_0 = 0) \tag{2.48}$$

as stated.

2.6 The Poles

One reason for writing the equations of motion using the μ coordinate instead of θ is because it removes singularities from the equations that occur on the rotation axis. However, this does not take care of all problems there. There are still several terms in equations (2.30)–(2.35) containing factors of $(1-\mu^2)^{-1}$ which blows up at the poles. Specifically, there is one term in (2.31) and two terms in (2.35), one of which is in $\mathcal{M}$.

The relevant terms in (2.35) are

$$\frac{\mu}{r^2}\left(\frac{r^2}{1-\mu^2}\dot{\mu}^2 + e^{\rho-\gamma-2\alpha}\frac{b^2}{r^2(1-\mu^2)}\right).$$

These apparent singularities at the pole can be removed simply by substituting

$$\frac{r^2}{1-\mu^2}\dot{\mu}^2 + e^{\rho-\gamma-2\alpha}\frac{b^2}{r^2(1-\mu^2)} = e^{-(\rho+\gamma+2\alpha)}(1-\omega b)^2 - \dot{r}^2$$

determined from (2.40).

The only term to worry about then is

$$e^{\rho-\gamma}\frac{b}{r^2(1-\mu^2)},$$

appearing in (2.31). This term gets very large when the geodesic passes near the pole. This can be seen by considering that the azimuthal angle ϕ changes very rapidly when passing near the pole, and it changes instantaneously when passing directly over the pole. The value of this term is bounded from above as the pole is approached by a geodesic. Since $\mathcal{P}$ must be positive for real velocities (following from (2.40)), then (2.36) and (2.39) give

$$\begin{aligned}\frac{e^{\rho-\gamma}|b|}{r^2(1-\mu^2)} &\leq \frac{e^{-(\gamma+\rho)}(1-\omega b)^2}{|b|} \\ &\sim \frac{1}{|b|} \quad \text{for small } b.\end{aligned}$$

Geodesics that pass directly over the pole must have $b=0$ as can be seen from (2.43). So geodesics with initial conditions on the pole propagate according to the same equations with $b=0$. The initial direction is then determined by ϕ_0 and altitude h (see section 3.4.2 for a discussion of altitude). The rest of

the geodesics we calculate do not pass so near the pole that we need to take any other special care with this term. To deal with this problem properly, one may need to use Cartesian coordinates instead of spherical coordinates using methods such as those described by Alcubierre, et al. [2].

2.7 Numerical Solutions of the Geodesics

2.7.1 Embedded Runge-Kutta Pairs

The algorithms presented in this section are adapted from [12]. For further details, you may refer to this source.

The equations (2.30)–(2.35) are numerically solved using embedded Runge-Kutta pair algorithms. Consider the equations written in the form

$$\dot{\mathbf{x}}(\lambda) = \mathbf{f}(\mathbf{x}(\lambda)) \tag{2.49}$$

where $\mathbf{x}$ is the phase space vector

$$\mathbf{x} = (t, \phi, r, \mu, \dot{r}, \dot{\mu}).$$

A Runge-Kutta algorithm estimates the values $\mathbf{x}_n \approx \mathbf{x}(\lambda_n)$ for a finite set of values of λ:

$$\{\lambda = \lambda_n : n = 0 \ldots N\}.$$

The *step size* of step n is defined to be $k_n = \lambda_{n+1} - \lambda_n$. In general, Runge-Kutta algorithms for autonomous equations (that is, the independent variable λ does not appear in the equations) can be expressed in the form

$$\mathbf{x}_{n+1} = \mathbf{x}_n + k_n \sum_{i=1}^{s} b_i \mathbf{f}_i \tag{2.50}$$

where

$$\begin{aligned} \mathbf{f}_1 &= \mathbf{f}(\mathbf{x}_n), \\ \mathbf{f}_i &= \mathbf{f}(\mathbf{x}_n + k_n \sum_{j=1}^{i-1} a_{ij} f_j), \ i = 2, 3, \ldots, s. \end{aligned}$$

s is the number of stages, and a_{ij} and b_i are parameters of the algorithm. These coefficients are chosen in such a way as to minimize *local truncation*

error $\mathbf{t}_n$, defined to be

$$\mathbf{t}_{n+1} \equiv \mathbf{x}_n + k_n \sum_{i=1}^{s} b_i \mathbf{f}_i - \mathbf{x}_{n+1}. \tag{2.51}$$

It turns out that for any choice of the algorithm parameters s, a_{ij}, and b_i, the local truncation error may be expressed as

$$\mathbf{t}_{n+1} = \sum_{i=p+1}^{\infty} k_n^i \varphi_{i-1}(\mathbf{x}(\lambda_n)), \tag{2.52}$$

where the φ_i are called *Error functions*. Note that the local truncation error drops as the step size decreases. A Runge-Kutta algorithm is said to be of order p if $\mathbf{t}_{n+1} = O(k_n^{p+1})$. Although it is not always the case, one usually finds better accuracy with higher order methods. However, higher order algorithms require more stages and are therefore less efficient. So one must weigh the accuracy of higher order algorithms against the efficiency of methods of lower order.

When we allow the step size to adjust for each step, we require a method for determining their appropriate values. Suppose we calculated a step $\mathbf{x}_{n+1}$ with step size k_n using an order p method. One way to test that the step size we used was small enough to be effective would be to redo the calculation with a $(p-1)$-order method and compare the results to see that they are the same within some tolerance. It turns out that this can be accomplished without having to re-evaluate the functions $\mathbf{f}_i$ with new values of a_{ij} by using a Runge-Kutta embedded pair.

$$\begin{aligned}
\hat{\mathbf{x}}_{n+1} &= \hat{\mathbf{x}}_n + k_n \sum_{i=1}^{s} \hat{b}_i \mathbf{f}_i \\
\mathbf{x}_{n+1} &= \hat{\mathbf{x}}_n + k_n \sum_{i=1}^{s} b_i \mathbf{f}_i \\
\mathbf{f}_i &= \mathbf{f}(\hat{\mathbf{x}}_n + k_n \sum_{j=1}^{i-1} a_{ij} \mathbf{f}_j), \ i = 1, 2, 3, \ldots, s
\end{aligned} \tag{2.53}$$

Here, the hat on the $\mathbf{x}_n$ indicates the approximation was made using the higher order method (order p), and the $\mathbf{x}_n$ without the hat is calculated using the qth order algorithm. Normally, one uses $p = q + 1$ and designates the algorithm RK$p(q)$.

a_{ij}				$\hat{b}_i$	b_i
				$\hat{b}_1$	b_1
a_{21}				$\hat{b}_2$	b_2
a_{31}	a_{32}			$\hat{b}_3$	b_3
$\vdots$	$\vdots$	$\ddots$		$\vdots$	$\vdots$
a_{s1}	a_{s2}	$\cdots$	a_{ss-1}	$\hat{b}_s$	b_s

Figure 2.1: The modified Butcher table. It specifies an explicit formula for an embedded Runge-Kutta pair RK$p(q)$ used to approximate an autonomous set of differential equations.

An algorithm can conveniently be specified explicitly using a modified Butcher table (see figure 2.1). See figure 2.2 for three such algorithms. Using an embedded Runge-Kutta pair, we estimate the local error of step n to be

$$\delta_{n+1} = \mathbf{x}_{n+1} - \hat{\mathbf{x}}_{n+1} \tag{2.54}$$

and check that its norm $\|\delta_{n+1}\|$ is less than the specified tolerance T. If so, then the step is considered successfully calculated within tolerance and the step size for the next step is calculated using

$$k_{n+1} = \min\left\{10k_n, 0.9k_n\left(\frac{T}{\|\delta_{n+1}\|}\right)^{\frac{1}{p+1}}\right\}, \qquad \|\delta_{n+1}\| \leq T. \tag{2.55}$$

Any norm could be used here; I use the max norm.

If the estimated local error is not within tolerance, then the step must be rejected and recalculated using a smaller step size. The reduced step size is calculated using the same formula as for the new step size of accepted steps.

$$k_n^{\text{NEW}} = 0.9k_n^{\text{OLD}}\left(\frac{T}{\|\delta_{n+1}\|}\right)^{\frac{1}{p+1}}, \qquad \|\delta_{n+1}\| > T \tag{2.56}$$

It follows from (2.36) and (2.40) that $\mathcal{Q}$ given by (2.39) is positive along the path of all geodesics. However, it is not uncommon for steps of the calculated geodesics that are near $\mathcal{Q} = 0$ to extrapolate into the $\mathcal{Q} < 0$ region. To ensure this doesn't occur with a large step size, the step is rejected and the step size is reduced if $\mathcal{Q}$ is less than some small, negative quantity. In our implementation, this quantity had a value of 10^{-4}.

a_{ij}		$\hat{b}_i$	b_i
		$\frac{1}{6}$	$\frac{1}{2}$
$\frac{1}{2}$		$\frac{2}{3}$	0
-1	2	$\frac{1}{6}$	$\frac{1}{2}$

(a) RK3(2)

a_{ij}				$\hat{b}_i$	b_i
				$\frac{13}{96}$	$\frac{23}{192}$
$\frac{1}{5}$				0	0
0	$\frac{2}{5}$			$\frac{25}{48}$	$\frac{55}{96}$
$\frac{6}{5}$	$-\frac{12}{5}$	2		$\frac{25}{96}$	$\frac{35}{192}$
$-\frac{17}{8}$	5	$-\frac{5}{2}$	$\frac{5}{8}$	$\frac{1}{12}$	$\frac{1}{8}$

(b) RK4(3)

a_{ij}						$\hat{b}_i$	b_i
						$\frac{35}{384}$	$\frac{5179}{57600}$
$\frac{1}{5}$						0	0
$\frac{3}{40}$	$\frac{9}{40}$					$\frac{500}{1113}$	$\frac{7571}{16695}$
$\frac{44}{45}$	$-\frac{56}{15}$	$\frac{32}{9}$				$\frac{125}{192}$	$\frac{393}{640}$
$\frac{19372}{6561}$	$-\frac{25360}{2187}$	$\frac{64448}{6561}$	$-\frac{212}{729}$			$-\frac{2187}{6784}$	$-\frac{92097}{339200}$
$\frac{9017}{3168}$	$-\frac{355}{33}$	$\frac{46732}{5247}$	$\frac{49}{176}$	$-\frac{5103}{18656}$		$\frac{11}{84}$	$\frac{187}{2100}$
$\frac{35}{384}$	0	$\frac{500}{1113}$	$\frac{125}{192}$	$-\frac{2187}{6784}$	$\frac{11}{84}$	0	$\frac{1}{40}$

(c) RK5(4)

Figure 2.2: Embedded Runge-Kutta pairs.

2.7.2 Accuracy of the Algorithms

The accuracy of the solutions calculated by the RK pairs can be determined in several different ways. Although one may think that accuracy is guaranteed by enforcing $\|\delta_{n+1}\| \leq T$, it is not always clear what tolerance is necessary to achieve a desirable solution. Also, one can argue that both $\hat{\mathbf{x}}_{n+1}$ and $\mathbf{x}_{n+1}$ may contain mutual biases inherent in the algorithm that would allow the approximated solution to deviate significantly from the exact solution. We require independent methods to verify that this does not occur.

Of significance is the fact that the momentum constraint (2.40) is not used in the algorithms. Although it could be used in the code to further constrain the approximate solution, it is more useful as an independent error estimator defined by

$$\varepsilon^*_{n-1} = \left| \dot{r}_n^2 + \frac{r_n^2}{1-\mu_n^2}\dot{\mu}_n^2 - \mathcal{P}(r_n, \mu_n, \dot{r}_n, \dot{\mu}_n) \right|. \tag{2.57}$$

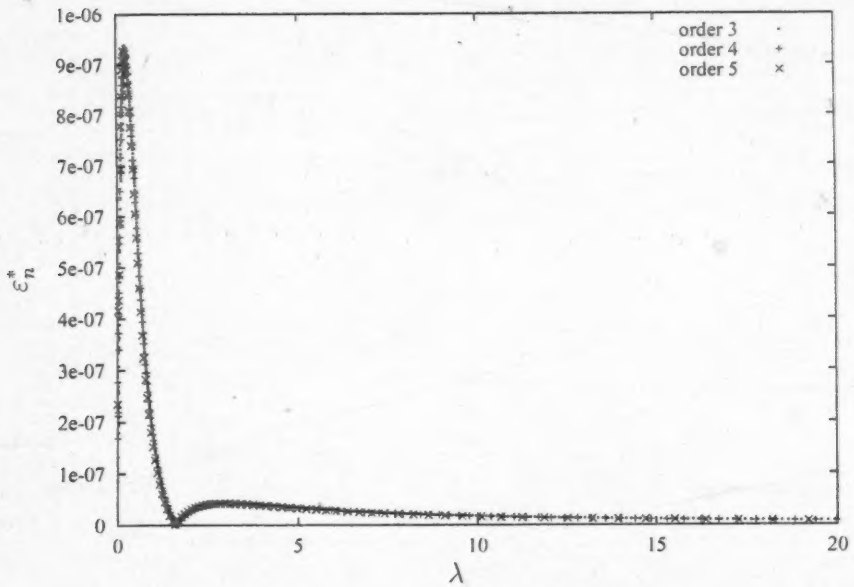

Figure 2.3: Plot of ε_n^* vs. λ_n for the three RK implementations. The plot actually continues until $\lambda \approx 205$, but ε_n^* remains less than 10^{-8} for $\lambda > 20$. The tolerances used were $T = 10^{-(p+4)}$ where p is the order of the algorithm. The star in this example has equation of state eos L, mass $M = 1.4M_\odot$, and frequency $f = 600$ Hz. The initial conditions of the geodesic are $s_0 = 0.5$, $\mu_0 = 0.5$, $\phi_0 = 0$, $\dot{r}_0 = 0.4$, $\dot{\mu}_0 = 0.1$, and $\dot{\phi}_s = +1$.

This is useful as an estimate of the accuracy of the solution at each step. We give initial conditions that satisfy the momentum constraint ($\varepsilon_{-1}^* = 0$) and then evolve without the constraint. Due to numerical errors, ε_n^* will not be zero for all of the evolution. Figure 2.3 shows a typical error profile for a geodesic. We can see that the profile is nearly identical for all three algorithms at the given tolerances. This is indeed a very common result, showing that the accuracy of the three algorithms are very similar.

A numerical integration of ε_n^*,

$$\varepsilon^* = \sum_{n=0}^{N-1} k_n \frac{\varepsilon_{n+1}^* + \varepsilon_n^*}{2}, \tag{2.58}$$

provides an error estimate for the geodesic.

For certain special cases, we can also determine the exact solution of the geodesic. There are currently two cases where this is possible: the star is

order of solver p	3	4	5
tolerance allowed T	10^{-7}	10^{-8}	10^{-9}
# of successfully calculated steps	927	260	138
# of rejected steps	0	0	0
estimated error value $\varepsilon^* \times 10^{-6}$	1.44017	1.44373	1.42615
processor time to calculate geodesic	0.08 s	0.03 s	0.02 s

Figure 2.4: Some statistics for the algorithms specified in figure 2.2 calculated for the geodesic described in figure 2.3.

non-rotating, or the star is rotating with the geodesic confined to the star's equatorial plane. In each of these cases, the theoretical geodesic is planar. So in these cases, there are two new error estimators we can calculate. The first tests that the geodesic is planar by calculating the coordinate angle the final position makes with the theoretical plane of motion. The second estimator is a comparison of the total angular sweep of the geodesic with the expected angular sweep. Before discussing these estimators, it is convenient to have some results from chapter 3 first. So these ideas are further discussed in section 3.5.

2.7.3 Comparison of Runge-Kutta Algorithms

This section discusses the three algorithms introduced in figure 2.2. Figure 2.4 lists some statistics for each algorithm for the geodesic described in figure 2.3. It is rare for the 3rd-order method to reject any steps, but quite common for the 5th-order method. Even so, the 5th-order algorithm appears to almost always compute fewer total steps (successful and rejected) than the other two algorithms. Since it is the most efficient algorithm and has little loss in accuracy, the 5th-order Runge-Kutta algorithm is used in all future calculations.

Chapter 3

Neutron Star Emissions

In order to determine how a neutron star appears from infinity, we must consider how photons travel from the surface of the star. For this task, the geodesics we consider in this section are those that originate on the surface of the star and travel away from the star. The purpose of this chapter is to explain how to calculate the mapping of geodesics originating from the star's surface to their ultimate destinations on the star's celestial sphere.

3.1 Parametrization of the Star's Surface

When the star is rotating, the surface is not a sphere. Instead, it is an oblate spheroid. The shape of the spheroid can be described by a function $r_s(\theta)$.

Because of azimuthal symmetry, we only need to consider those points of the surface at $\phi_0 = 0$, and because of mirror symmetry about the equatorial plane, we only need $\theta_0 \leq \frac{\pi}{2}$ as depicted in figure 3.1.

We quantize the stellar surface that we are considering with the set of points

$$\{\mu = \mu_i = \cos\theta_i : \theta_i = \frac{\pi}{2} - i\Delta\theta;\ i = 0, 1, ..., N_\theta\} \tag{3.1}$$

where $\Delta\theta$ is a small constant and $\theta_{N_\theta} \geq 0$ (see Figure 3.1). Restricting to $\theta_{N_\theta} > 0$ can be used to avoid difficulties with geodesics too near the polar regions. The calculations shown in this manuscript all used $\theta_{N_\theta} = 0$.

It will be useful to consider the tangent to the surface at the latitude θ_i. Given a position $(r_s(\theta_0), \theta_0)$ on the surface, there is a surface parameter $K(\theta_0)$

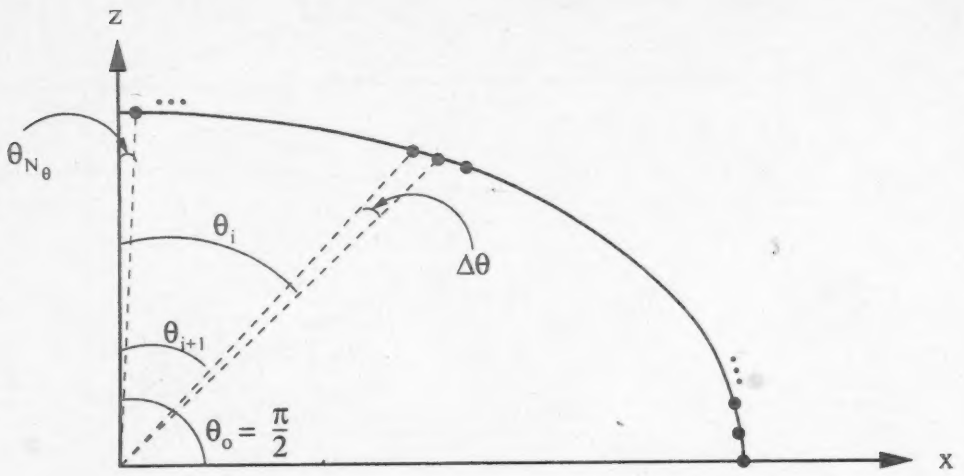

Figure 3.1: The points considered on the surface of a neutron star are separated by a small polar angle $\Delta\theta$. This picture shows an example where $\theta_{N_\theta} > 0$.

given by

$$\frac{1}{r_0}\frac{dr_s}{d\theta}\bigg|_{\theta=\theta_0} = K(\theta_0). \tag{3.2}$$

The curve of the surface is such that $K \geq 0$ with K vanishing at the pole and equator: $K(0) = K(\frac{\pi}{2}) = 0$. If the star were not rotating, $K(\theta_0) = 0$ for $0 \leq \theta_0 \leq \frac{\pi}{2}$. Our numerical code computes the location of the star's surface and the function K.

In Cartesian coordinates, $z = r\cos\theta$ and $x = r\sin\theta$, the slope of the tangent to the surface at point θ_i is given by

$$m_i = -\tan\theta_i \left(\frac{1 - \cot\theta_i K_i}{1 + \tan\theta_i K_i}\right). \tag{3.3}$$

3.2 Emission Directions in Curved Space: $D - \dot{\phi}_0$ Parametrization

Given an initial position on the surface of the neutron star, we need a way of describing those 4-velocities that travel away from the star.

Directions in the $r\mu$-plane may be described by the curves

$$\frac{\sqrt{1-\mu_0^2}}{r_0}\frac{dr}{d\mu}\bigg|_{\mu=\mu_0} = -\frac{1}{r_0}\frac{dr}{d\theta}\bigg|_{\theta=\theta_0} = D \tag{3.4}$$

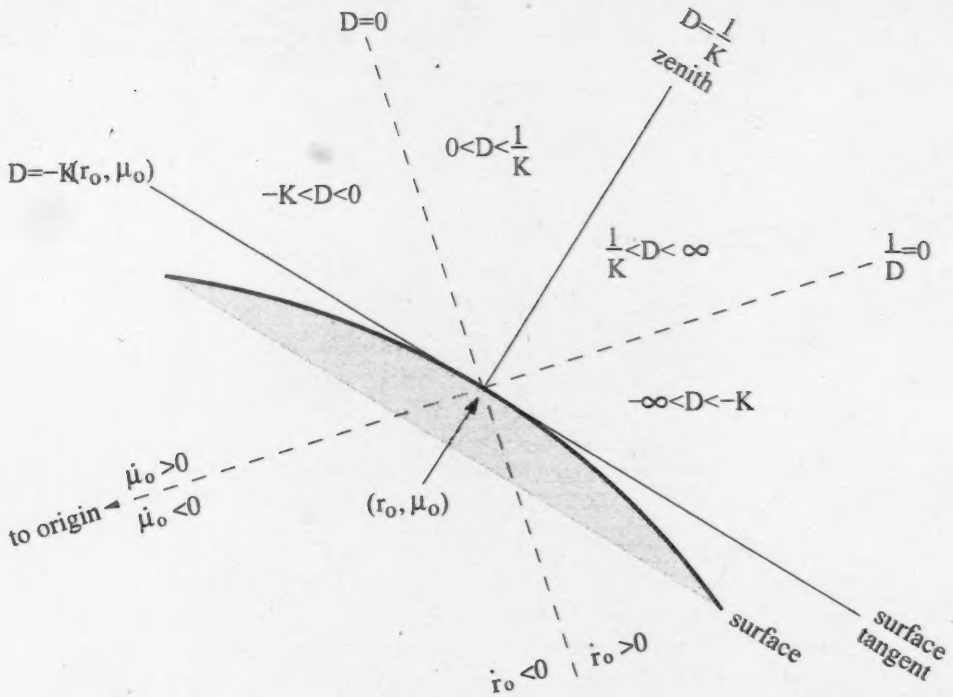

Figure 3.2: Parametrizing the directions away from a point of the surface with D.

for any real-valued constant D, where $(r_0,\ \mu_0)$ is the initial position on the surface of the star. Figure 3.2 shows how the value of D specifies a direction in the $r\mu$-plane.

So we can see that to fully specify an initial 4-velocity, we only need to specify

$$\frac{r_0}{\sqrt{1-\mu_0^2}} D = \left.\frac{dr}{d\mu}\right|_{\lambda=0} = \frac{\dot{r}_0}{\dot{\mu}_0} \tag{3.5}$$

and $\dot{\phi}_0$. In order to recover the original initial conditions, I will now demonstrate how one determines b, $\dot{r}_0$, and $\dot{\mu}_0$ from D and $\dot{\phi}_0$. From (2.31) and (2.46),

$$b = \frac{d_0^2}{1-v_0^2}\left(e^{-(\gamma_0+\rho_0)}\dot{\phi}_0 - \omega_0\right). \tag{3.6}$$

From (3.5) and (2.40) we can solve for the remaining initial conditions:

$$\dot{r}_0^2 = \frac{\mathcal{P}_0 D^2}{1+D^2} \tag{3.7}$$

$$\dot{\mu}_0^2 = \frac{1-\mu_0^2}{r_0^2}\frac{\mathcal{P}_0}{1+D^2} \tag{3.8}$$

with

$$\begin{aligned}\mathcal{P}_0 &= e^{-(2\alpha_0+\gamma_0+\rho_0)}\left[(1-\omega_0 b)^2 - \frac{b^2}{d_0^2}\right] \\ &= e^{-(2\alpha_0+\gamma_0+\rho_0)}\frac{1-e^{2(\gamma_0+\rho_0)}d_0^2\dot{\phi}_0^2}{1-v_0^2} \qquad (3.9)\end{aligned}$$

where I used (3.6). The sign of $\dot{r}_0$ and $\dot{\mu}_0$ can be determined from the position in figure 3.2:

$$\dot{r}_0 = \epsilon D\sqrt{\frac{\mathcal{P}_0}{1+D^2}} \qquad (3.10)$$

$$\dot{\mu}_0 = \epsilon\frac{\sqrt{1-\mu_0^2}}{r_0}\sqrt{\frac{\mathcal{P}_0}{1+D^2}} \qquad (3.11)$$

$$\epsilon = \begin{cases} 1, & D > -K \\ -1, & D < -K \end{cases}. \qquad (3.12)$$

Figure 3.2 illustrates that ϵ can have either value when $D = -K$ (the geodesic is along the horizon).

In the $D\dot{\phi}_0$-parametrization, we have seen that D can take any extended real value; however, $\dot{\phi}_0$ has finite bounds. The extreme values of $\dot{\phi}_0$ occur when $\dot{r}_0 = \dot{\mu}_0 = 0$. Then from (2.40), we can determine the extreme impact parameters $b_\pm$.

$$\begin{aligned}&\mathcal{P}_0 = 0 \\ \Longrightarrow\ &(1-\omega_0 b_\pm)^2 - \frac{b_\pm^2}{d_0^2} = 0 \\ \Longrightarrow\ &b_\pm = \frac{d_0}{v_0 \mp 1} \qquad (3.13)\end{aligned}$$

Substituting into (2.31) gives the extreme values of $\dot{\phi}_0$ being

$$\begin{aligned}\dot{\phi}_{o\pm} &= e^{-(\gamma_0+\rho_0)}\left(\omega_0 + \frac{1-v_0^2}{d_0^2}b_\mp\right) \\ &= e^{-(\gamma_0+\rho_0)}\left(\omega_0 - \frac{v_0 \mp 1}{d_0}\right) \\ &= \pm\frac{1}{d_0}e^{-(\gamma_0+\rho_0)}. \qquad (3.14)\end{aligned}$$

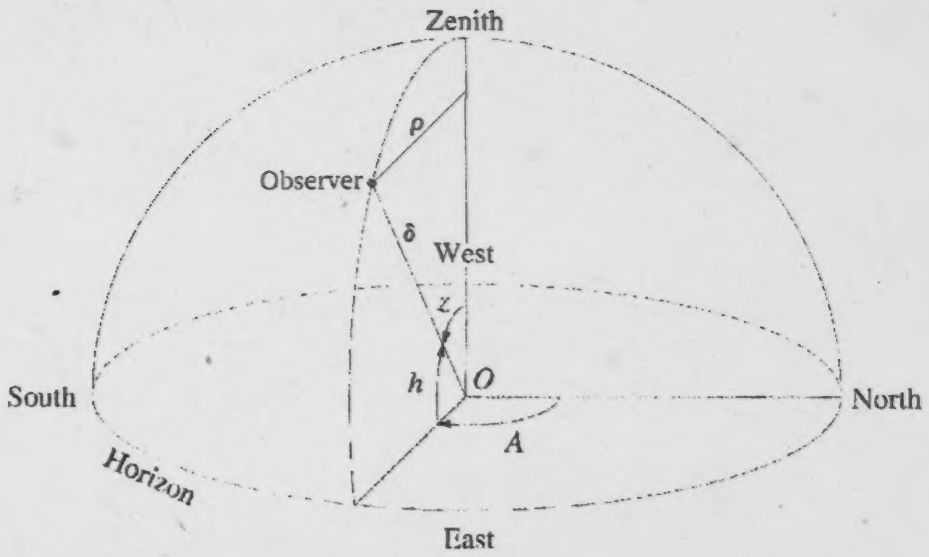

Figure 3.3: The altitude-azimuth $(h - A)$ coordinate system. Also shown in this diagram is the zenith angle z, hemisphere radius δ, and cylindrical radius ρ. (Figure adapted from Carroll and Ostlie [8]).

3.3 Altitude-Azimuth Coordinate System in Flat Space

Although the $D\dot{\phi}_0$-parametrization of directions is valid, it is not as natural for describing emissions from the surface of a star as the altitude-azimuth system. Before describing how to develop such a system in curved space, I review the coordinates in flat space.

Consider a specific point on the surface. Photons can be emitted into any direction away from the star. Imagine a sphere of radius $\delta \ll 1$ centered on the point on the surface. This sphere is separated into two hemispheres by the star's surface. Each point on the hemisphere outside the star represents a different direction of propagation for photons. So to quantize the initial propagation directions, we only need to quantize the hemisphere. This is easily done with an altitude-azimuth system shown in figure 3.3. The initial direction has an altitude angle h, the angle above the horizon, and azimuth angle A, the angle along the horizon that is east from north [8].

3.4 Altitude-Azimuth Coordinate System in Curved Space

In order to introduce an altitude-azimuth coordinate system for a neutron star, we need to define the concept of an angle between two vectors in a curved space. In flat space, the cosine of an angle is the inner product of two 3-vectors. We can make a similar definition by projecting a 4-vector into a three-dimensional spacelike surface. We begin this section by introducing a projection operator that will allow us to define altitude and azimuth angles.

3.4.1 A Spacelike 3-Metric for a Neutron Star

The equation describing a null geodesic can be rewritten in a form which will motivate a choice of a spacelike 3-metric.

Solve (2.31) for b and substitute the result into (2.40). After a little algebra, the resulting equation is

$$e^{2\alpha+\gamma+\rho}(1-e^{-2\rho}\omega^2 r^2(1-\mu^2))\left(\dot{r}^2+\frac{r^2}{1-\mu^2}\dot{\mu}^2\right)+e^{2\gamma}r^2(1-\mu^2)\dot{\phi}^2=1. \quad (3.15)$$

In terms of the 4-metric (2.2), this equation reads

$$-g_{tt}(g_{rr}\dot{r}^2+g_{\mu\mu}\dot{\mu}^2)-(g_{tt}g_{\phi\phi}-g_{t\phi}^2)\dot{\phi}^2=1. \quad (3.16)$$

So we define the 3-metric ${}^3g_{ij}$ by

$${}^3g_{rr}\equiv -g_{tt}g_{rr}=e^{2\alpha+\gamma+\rho}(1-v^2) \quad (3.17)$$

$${}^3g_{\mu\mu}\equiv -g_{tt}g_{\mu\mu}=e^{2\alpha+\gamma+\rho}(1-v^2)\frac{r^2}{1-\mu^2} \quad (3.18)$$

$${}^3g_{\phi\phi}\equiv -g_{tt}g_{\phi\phi}+g_{t\phi}^2=e^{2(\gamma+\rho)}\frac{v^2}{\omega^2} \quad (3.19)$$

with all other components equal to zero and where v is defined by

$$v\equiv e^{-\rho}\omega r\sqrt{1-\mu^2}. \quad (3.20)$$

Then (3.15) is simply the normalization of the 3-vector

$${}^3g_{ij}\frac{dx^i}{d\lambda}\frac{dx^j}{d\lambda}=1 \quad (3.21)$$

which embodies the constancy of the speed of light in curved space-time.

In light of this result, formulae such as (2.48) and (3.14) are now nearly trivial and are much more simple to derive.

It is common (see for example problem 31 in chapter 3 of Schutz [29]) for 3-metrics to be calculated from the projection tensor

$$h_{ab} = g_{ab} + u_a u_b$$

where u_a is the 4-velocity of some timelike observer. The choice of observer is arbitrary, but a simple choice is that of an object at rest with $u^a = u^t t^a$ where $u_a u^a = -1$ requires

$$\left(u^t\right)^2 = -\frac{1}{g_{tt}}.$$

Comparing with (3.17)–(3.19) shows that

$${}^3g_{ab} = -g_{tt} h_{ab}.$$

We can now use this 3-metric to define angles in the neighborhood of the neutron star. Given two trajectories $\frac{dx_1^i}{d\lambda}$ and $\frac{dx_2^i}{d\lambda}$ in space propagating away from the same point, the angle φ between them is given by

$$\cos\varphi = {}^3g_{ij} \frac{dx_1^i}{d\lambda} \frac{dx_2^j}{d\lambda}. \tag{3.22}$$

This is equivalent to the definition of angle given in [26].

3.4.2 Altitudes from a Neutron Star Surface

In flat space-time, the altitude h is related to the angle z from the zenith (ie. the zenith angle) by (see figure 3.3)

$$h = \frac{\pi}{2} - z. \tag{3.23}$$

The values of D and $\dot{\phi}_0$ that give the zenith direction are

$$D_z = \frac{1}{K}, \tag{3.24}$$

$$\dot{\phi}_{o_z} = 0. \tag{3.25}$$

From (3.9)–(3.12) we find the rest of the initial speed components along the zenith.

$$\dot{r}_{o_z} = \sqrt{\frac{\mathcal{P}_{o_z}}{1+K^2}} \tag{3.26}$$

$$\dot{\mu}_{o_z} = \frac{\sqrt{1-\mu_0^2}}{r_0}\sqrt{\frac{K^2\mathcal{P}_{o_z}}{1+K^2}} \tag{3.27}$$

$$\mathcal{P}_{o_z} = e^{-(2\alpha_0+\gamma_0+\rho_0)}\frac{1}{1-v_0^2} \tag{3.28}$$

So from (3.22), the zenith angle is given by

$$\begin{aligned}\cos z &= {}^3g_{ij}\frac{dx^i}{d\lambda}\frac{dx_z^j}{d\lambda} \\ &= \epsilon e^{(2\alpha_0+\gamma_0+\rho_0)}(D+K)(1-v_0^2)\sqrt{\frac{\mathcal{P}_0\mathcal{P}_{o_z}}{(1+D^2)(1+K^2)}} \\ &= \epsilon\sqrt{1-e^{2(\gamma_0+\rho_0)}d_0^2\dot{\phi}_0^2}\,\frac{D+K}{\sqrt{(1+D^2)(1+K^2)}}.\end{aligned} \tag{3.29}$$

At the zenith,

$$\cos z = \frac{-\frac{1}{K}+K}{\sqrt{(1+\frac{1}{K^2})(1+K^2)}} = 1 \implies z = 0$$

and along the horizon where $D = -K$,

$$\cos z = 0 \implies z = \frac{\pi}{2}.$$

With these results, it makes sense for (3.23) to apply. So altitudes can be expressed as

$$\sin h = \epsilon\sqrt{1-e^{2(\gamma_0+\rho_0)}d_0^2\dot{\phi}_0^2}\,\frac{D+K}{\sqrt{(1+D^2)(1+K^2)}}. \tag{3.30}$$

3.4.3 Azimuth Angles on the Neutron Star Horizon

Existence of Azimuth Angles

In order to investigate the feasibility of azimuth angles in our curved space, we need to understand contours $D_h(\dot{\phi}_0)$ of constant altitude and their lengths on the direction hemisphere depicted in figure 3.3. Whether or not a useful definition of azimuth angle is found, the proper lengths of the contours will be required in order to add evenly separated points to them.

To solve for the contours of constant altitude, we pose the following: given a fixed altitude h, what is the value of D for each allowed value of $\dot{\phi}_0$? To answer this question, define

$$\xi(\dot{\phi}_0) \equiv \frac{\sin h}{\sqrt{1 - e^{2(\gamma_0+\rho_0)} d_0^2 \dot{\phi}_0^2}} \geq 0. \tag{3.31}$$

Squaring (3.30) gives (after a little manipulation)

$$(1 + D^2)(1 + K^2)\xi^2 = (D + K)^2$$

and we simply apply the quadratic formula to solve for D:

$$D = \frac{K + s(1 + K^2)\xi\sqrt{1 - \xi^2}}{(1 + K^2)\xi^2 - 1} \qquad \text{Contour of Constant Altitude} \tag{3.32}$$

where

$$s = \pm 1.$$

The two signs in this equation reflect the two paths that can be taken when following the contour from the lowest to highest allowed values of $\dot{\phi}_0$. One path would have D taking values from $\frac{1}{K}$ to $-K$ and back to $\frac{1}{K}$ again as $\dot{\phi}_0$ increases. The second path would have $\frac{1}{D}$ go from K to $-\frac{1}{K}$ and back again. Since the first path contains $D = 0$, this can only occur if we use the '$-$' sign in (3.32). Therefore,

$$s = \begin{cases} +1 & \text{when } -\frac{1}{K} \leq \frac{1}{D} < K \\ -1 & \text{when } -K \leq D < \frac{1}{K} \end{cases} \tag{3.33}$$

For a given altitude, the allowed values of $\dot{\phi}_0$ are determined by the radicand in (3.32) which requires $\xi^2 \leq 1$, or

$$\dot{\phi}_0^2 \leq e^{-2(\gamma_0+\rho_0)} \frac{\cos^2 h}{d_0^2} = \frac{\cos^2 h}{{}^3g_{\phi\phi}}. \tag{3.34}$$

This is consistent with (3.14).

When calculating D using (3.32), there are two special cases that require attention. First, when $s = -1$, D is finite for all values of $\dot{\phi}_0$. So the denominator vanishing at $\xi^2 = \frac{1}{1+K^2}$ must only be an apparent singularity. We can

resolve this by doing a perturbation expansion

$$\begin{aligned} D &= \frac{1-K^2}{2K} + \frac{(1+K^2)^2}{8K^3}[\xi^2(1+K^2)-1] \\ &+ \frac{(1+K^2)^2(1-K^2)}{16K^5}[\xi^2(1+K^2)-1]^2 \\ &+ \frac{(1+K^2)^2}{128K^7}(5K^4-6K^2+5)[\xi^2(1+K^2)-1]^3 \\ &+ O\{[\xi^2(1+K^2)-1]^4\} \end{aligned} \tag{3.35}$$

when $|\xi^2(1+K^2)-1| \ll 1$. The second special case occurs when $\frac{1}{D}$ is being calculated (usually when $s=+1$). Then we have another small denominator problem when both $K \ll 1$ and $1-\xi \ll 1$. A perturbative expansion of $\frac{1}{D}$ about $K=0$ is very simple when we notice

$$\begin{aligned} \frac{1}{D} - \frac{s\sqrt{1-\xi^2}}{\xi} &= \frac{\xi^2(1+K^2)-1}{K - s(1+K^2)\xi\sqrt{1-\xi^2}} - \frac{s\sqrt{1-\xi^2}}{\xi} \\ &= \frac{K}{\xi^2}\frac{1}{1-\frac{s\sqrt{1-\xi^2}}{\xi}K} \\ &= \frac{K}{\xi^2}\sum_{n=0}^{\infty}\left(\frac{s\sqrt{1-\xi^2}}{\xi}K\right)^n. \end{aligned}$$

Then

$$\frac{1}{D} = \frac{s\sqrt{1-\xi^2}}{\xi} + \sum_{n=0}^{\infty} s^n \frac{(1-\xi^2)^{n/2}}{\xi^{n+2}} K^{n+1}. \tag{3.36}$$

This sum may be truncated after a few terms when $K \ll 1$ and $1-\xi \ll 1$.

With the contours of constant altitude written the way they are in (3.32), we can consider D to be parametrized by ξ instead of $\dot{\phi}_0$. From (3.31) we can see that ξ is an even function of $\dot{\phi}_0$. By also considering (3.34), we can see that as $\dot{\phi}_0$ increases from its minimum value to 0, ξ decreases from 1 to $\sin h$. ξ then increases from $\sin h$ to 1 again as $\dot{\phi}_0$ continues from 0 to its maximum value.

Now consider the contour of constant altitude on the hemisphere of radius δ about the initial position on the star's surface as depicted in figure 3.3.[1] The

[1] In a curved spatial background, one can generate the surface of a hemisphere of radius δ by fixing one end of a rod of length δ and allowing the other end to move freely, sweeping out a spherical surface.

coordinates x_c^i of the contour, parametrized by ξ, are

$$x_c^i(\xi) = x_0^i + \delta \dot{x}_0^i(\xi).$$

Apply (3.9)–(3.11) followed by (3.31) to determine r_c and μ_c, and just use (3.31) for ϕ_c (recall $\dot{\phi}_s$ is given by (2.42)).

$$\begin{aligned}
r_c(\xi) &= r_0 + \delta \dot{r}(\xi) \\
&= r_0 + \delta\epsilon D(\xi)\sqrt{\frac{e^{-(2\alpha_0+\gamma_0+\rho_0)}\left(1 - e^{2(\gamma_0+\rho_0)}d_0^2\dot{\phi}_0^2\right)}{(1-v_0^2)[1+D^2(\xi)]}} \\
&= r_0 + e^{-\alpha_0-(\gamma_0+\rho_0)/2}\frac{\delta\epsilon}{\sqrt{1-v_0^2}}\frac{\sin h}{\xi}\frac{D(\xi)}{\sqrt{1+D^2(\xi)}} \qquad (3.37) \\
\mu_c(\xi) &= \mu_0 + \delta\dot{\mu}(\xi) \\
&= \mu_0 + \delta\epsilon\frac{\sqrt{1-\mu_0^2}}{r_0}\sqrt{\frac{e^{-(2\alpha_0+\gamma_0+\rho_0)}\left(1 - e^{2(\gamma_0+\rho_0)}d_0^2\dot{\phi}_0^2\right)}{(1-v_0^2)[1+D^2(\xi)]}} \\
&= \mu_0 + \frac{\sqrt{1-\mu_0^2}}{r_0}e^{-\alpha_0-(\gamma_0+\rho_0)/2}\frac{\delta\epsilon}{\sqrt{1-v_0^2}}\frac{\sin h}{\xi}\frac{1}{\sqrt{1+D^2(\xi)}} \qquad (3.38) \\
\phi_c(\xi) &= \delta\dot{\phi}_0 \\
&= \dot{\phi}_s\delta e^{-(\gamma_0+\rho_0)}\frac{1}{d_0}\sqrt{1-\frac{\sin^2 h}{\xi^2}} \qquad (3.39)
\end{aligned}$$

In flat space-time, the length of a contour of constant altitude h on a hemisphere of radius δ is $C = 2\pi\delta\cos h$ where 2π represents the azimuth angle subtended by the contour. The proper length of the contour in curved space-time is [20]

$$C = \int \left|{}^3g_{ij}\frac{dx_c^i}{d\xi}\frac{dx_c^j}{d\xi}\right|^{\frac{1}{2}} d\xi \qquad (3.40)$$

integrated over the length of the contour. Running along the contour beginning at the position where $\dot{\phi}_0$ has its minimum value, the value of ξ goes from 1 to $\sin h$ and back to 1 twice. It follows that to calculate C, we must integrate over ξ from $\sin h$ to 1 four times. After some work, we have

$${}^3g_{ij}\frac{dx_c^i}{d\xi}\frac{dx_c^j}{d\xi} = \frac{\delta^2\sin^2 h}{\xi^2}\left(\frac{1}{1-\xi^2} + \frac{1}{\xi^2 - \sin^2 h}\right). \qquad (3.41)$$

Therefore,

$$C = 4\delta\sin h\int_{\sin h}^{1}\frac{1}{\xi}\sqrt{\frac{1}{1-\xi^2} + \frac{1}{\xi^2-\sin^2 h}}d\xi. \qquad (3.42)$$

With the substitution

$$\Pi = \frac{1 + \left(1 - \frac{2}{\xi^2}\right) \sin^2 h}{\cos^2 h} \tag{3.43}$$

the integration becomes

$$C = 2\delta \cos h \int_{-1}^{1} \frac{d\Pi}{\sqrt{1 - \Pi^2}} \tag{3.44}$$

$$= 2\pi\delta \cos h. \tag{3.45}$$

Remarkably, we arrive at the classical result. Since the contour of constant altitude sweeps a total angle of 2π, we have motivation to find a quantity that has the interpretation of azimuth angle.

Definition of Azimuth Angles

Since the azimuth angle is an angle between directions *in the horizon*, we need a way to "project" a direction into the horizon. Consider a direction with values of D and $\dot{\phi}_0$. From figure 3.3, projection into the horizon obviously involves setting $D = -K$, but how is $\dot{\phi}_0$ adjusted?

The north direction is characterized by $A = 0$. The value of $\dot{\phi}_0$ for all altitudes in the northerly direction is 0. In the easterly direction, $A = \frac{\pi}{2}$ and $\dot{\phi}_0$ has the maximum allowed value for the altitude h of the direction. From (3.34),

$$\dot{\phi}_0 = e^{-(\gamma_0 + \rho_0)} \frac{\cos h}{d_0} \tag{3.46}$$

for the east direction at altitude h. So in the case of the east direction, the projection is made by keeping $\frac{\dot{\phi}_0}{\cos h}$ constant.

Trying this prescription for each direction suggests we "project" directions into the horizon using the projection operation

$$D \xrightarrow{P} D_P = -K, \tag{3.47}$$

$$\dot{\phi}_0 \xrightarrow{P} \dot{\phi}_{0P} = \frac{\dot{\phi}_0}{\cos h}. \tag{3.48}$$

Then from (3.9)-(3.11), the projected values of $\dot{r}_0$ and $\dot{\mu}_0$ into the horizon are

$$\dot{r}_{0P} = \epsilon e^{-\alpha_0 - (\gamma_0 + \rho_0)/2} \frac{-K}{\sqrt{1 + K^2}} \sqrt{\frac{1 - e^{2(\gamma_0 + \rho_0)} \frac{d_0^2 \dot{\phi}_0^2}{\cos^2 h}}{1 - v_0^2}}, \tag{3.49}$$

$$\dot{\mu}_{0P} = \epsilon \frac{\sqrt{1 - \mu_0^2}}{r_0} e^{-\alpha_0 - (\gamma_0 + \rho_0)/2} \frac{1}{\sqrt{1 + K^2}} \sqrt{\frac{1 - e^{2(\gamma_0 + \rho_0)} \frac{d_0^2 \dot{\phi}_0^2}{\cos^2 h}}{1 - v_0^2}}. \tag{3.50}$$

The azimuth angle is the angle between a direction projected into the horizon, and the north direction in the horizon. The north direction is the horizon is that where $\dot{\phi}_0 = 0$ and $\epsilon = +1$. So denoting the zero-azimuth direction by $\dot{x}^i_{o_h}$, it is given by

$$\dot{r}_{o_h} = \frac{-e^{-\alpha_0-(\gamma_0+\rho_0)/2}K}{\sqrt{(1-v_0^2)(1+K^2)}} \tag{3.51}$$

$$\dot{\mu}_{o_h} = \frac{\sqrt{1-\mu_0^2}}{r_0}\frac{e^{-\alpha_0-(\gamma_0+\rho_0)/2}}{\sqrt{(1-v_0^2)(1+K^2)}} \tag{3.52}$$

$$\dot{\phi}_{o_h} = 0 \tag{3.53}$$

allowing us to determine the azimuth angle A.

$$\cos A = {}^3g_{ij}\dot{x}^i_{o_h}\dot{x}^j_{o_P} \tag{3.54}$$

$$= \epsilon\sqrt{1-e^{2(\gamma_0+\rho_0)}\frac{d_0^2\dot{\phi}_0^2}{\cos^2 h}} \tag{3.55}$$

It is more convenient to express the azimuth angle as

$$\sin A = e^{\gamma_0+\rho_0}\frac{d_0\dot{\phi}_0}{\cos h} \tag{3.56}$$

which has the same sign as $\dot{\phi}_0$.

Verification of Azimuth Definition

This result depends on our having properly chosen the projection operator (3.48). To see that A does indeed have the interpretation of azimuth angle, calculate the length of a sector S of constant altitude h from zero-azimuth to some arbitrary azimuthal angle $A^* \leq \frac{\pi}{2}$. Following the calculation of C in the last section, we can use (3.56) in (3.31) to get

$$\xi(A) = \frac{\sin h}{\sqrt{1-\cos^2 h\sin^2 A}}. \tag{3.57}$$

Then

$$S = \delta\sin h\int_{\sin h}^{\xi^*}\frac{1}{\xi}\sqrt{\frac{1}{1-\xi^2}+\frac{1}{\xi^2-\sin^2 h}}d\xi \tag{3.58}$$

where $\xi^* = \xi(A^*)$. Using the same substitution (3.43), the upper bound becomes

$$\begin{aligned} \Pi^* &= \frac{1 + \left(1 - 2\frac{1-\cos^2 h \sin^2 A^*}{\sin^2 h}\right)\sin^2 h}{\cos^2 h} \\ &= 2\sin^2 A^* - 1 \\ &= -\cos 2A^* \end{aligned}$$

and the sector length is

$$\begin{aligned} S &= \frac{\delta}{2}\cos h \int_{-1}^{-\cos 2A^*} \frac{d\Pi}{\sqrt{1-\Pi^2}} \\ &= \frac{\delta}{2}\cos h \int_{\cos 2A^*}^{1} \frac{d\Pi}{\sqrt{1-\Pi^2}} \\ &= \frac{\delta}{2}\cos h \left[\frac{\pi}{2} - \sin^{-1}(\cos 2A^*)\right] \\ &= A^*\delta\cos h \end{aligned} \tag{3.59}$$

where the second line took advantage of the integrand being an even function and the last line used $0 < A^* \leq \frac{\pi}{2}$. This is the result expected for if A is the azimuth angle.

3.4.4 Discretization of the Altitude-Azimuth System

One way to break up this domain would be to choose altitudes evenly spaced by Δh, and choose an azimuth spacing ΔA_j for each altitude h_j so that all the points on the hemisphere are approximately uniformly spaced. Under this scheme, the set of altitudes would be

$$\{h = h_j = j\Delta h : \ j = 0, 1, ..., N_h; \ h_{N_h} = \frac{\pi}{2}\}. \tag{3.60}$$

Keeping the points on the sphere approximately equidistant requires ΔA_j to satisfy

$$\rho_j \Delta A_j \approx \delta \Delta h \tag{3.61}$$

where ρ_j is the radius of the circle of constant altitude h_j (see figure 3.3). That is,

$$\rho_j = \delta \cos h_j \tag{3.62}$$

and so

$$\Delta A_j \approx \frac{\Delta h}{\cos h_j}. \tag{3.63}$$

Let M_j be the number of points added to the hemisphere at altitude h_j under this prescription. Since

$$\begin{aligned} M_j &= \frac{\text{length of circle of constant altitude } h_j}{\text{length between each point on the circle}} \\ &= \frac{2\pi\rho_j}{\rho_j \Delta A_j} \\ &= \frac{2\pi}{\Delta A_j} \end{aligned} \tag{3.64}$$

which must be a natural number. This motivates the following procedure for determining ΔA_j. Let

$$M_j = \left\lceil \frac{2\pi \cos h_j}{\Delta h} \right\rceil \tag{3.65}$$

where the ceiling operator is defined by $\lceil x \rceil = n$ with n being the integer satisfying $n - 1 < x \leq n$. Then (3.64) gives us

$$\Delta A_j = \frac{2\pi}{M_j}. \tag{3.66}$$

So the set of azimuth angles at a given altitude h_j would be

$$\{A_{jk} = j\Delta A_j + A_R : \ k = 0, 1, ..., M_j - 1\}. \tag{3.67}$$

Here, A_R is a pseudo-randomly chosen value between 0 and ΔA_j. Its purpose is to prevent the introduction of artificial structure in the distribution of photons from having a point at $A_j = 0$ for all altitudes h_j.

Although this method of covering the hemisphere is simple, it has some shortcomings. For instance, geodesics with small altitudes change more rapidly with respect to altitude than geodesics initially near the zenith. As an example, geodesics that orbit the star several times before escaping to infinity will travel to very different positions at infinity with very small changes in altitude with which the photon leaves the surface. With this in mind, one should choose altitudes to be more closely spaced near the horizon than at the zenith. One such scheme is to separate the altitudes evenly in $\sin h_j$. If we denote this separation by Δs, then the values of altitude are

$$\{h_j = \sin^{-1}(j\Delta s) : \ i = 0, 1, ..., N_h; \ h_{N_h} = \frac{\pi}{2}\}. \tag{3.68}$$

The azimuth angles are separated evenly by an approximate average separation of points on the hemisphere. As with (3.61),

$$\rho_i \Delta A_j \approx \delta \overline{\Delta h} \tag{3.69}$$

where $\overline{\Delta h}$ is the average change in altitude. Noting that $\Delta s = N_h^{-1}$, then

$$\begin{aligned}
\overline{\Delta h} &= \frac{1}{N_h} \sum_{j=1}^{N_h} (h_j - h_{j-1}) \\
&= \Delta s \sum_{j=1}^{N_h} \left[\sin^{-1}\left(\frac{j}{N_h}\right) - \sin^{-1}\left(\frac{j-1}{N_h}\right) \right] \\
&= \Delta s [\sin^{-1} 1 - \sin^{-1} 0] \\
&= \frac{\pi}{2} \Delta s.
\end{aligned} \tag{3.70}$$

So following the same method as with the first prescription, the azimuth angles with this prescription are

$$\{A_{jk} = j\Delta A_j + A_R : \ k = 0, 1, ..., M_j - 1\} \tag{3.71}$$

where in this case,

$$M_j = \left\lceil \frac{4 \cos h_j}{\Delta s} \right\rceil. \tag{3.72}$$

3.4.5 Summary of the Altitude-Azimuth System

Now that we have defined the concepts of altitude and azimuth angles in our curved space background, we can choose directions leaving the star by choosing values of these angles just as we would for flat space-time discussed at the beginning of this chapter. Values of altitude h and azimuth A angles are chosen using (3.68) and (3.71), respectively.

We then convert h and A to the initial velocity conditions required in section 2.5 by using

$$\dot{r}_0 = \epsilon e^{-\alpha_0 - (\gamma_0 + \rho_0)/2} \frac{D}{\sqrt{1 + D^2}} \sqrt{\frac{1 - \cos^2 h \sin^2 A}{1 - v_0^2}} \tag{3.73}$$

$$\dot{\mu}_0 = \epsilon \frac{\sqrt{1 - \mu_0^2}}{r_0} e^{-\alpha_0 - (\gamma_0 + \rho_0)/2} \frac{1}{\sqrt{1 + D^2}} \sqrt{\frac{1 - \cos^2 h \sin^2 A}{1 - v_0^2}} \tag{3.74}$$

$$\dot{\phi}_0 = e^{-\gamma_0} \frac{\cos h \sin A}{r_0 \sqrt{1 - \mu_0^2}} \tag{3.75}$$

where

$$\epsilon = \begin{cases} \text{sign}(D+K) & \text{when } D+K \neq 0 \\ \text{sign}(\cos A) & \text{when } D+K = 0 \end{cases} \tag{3.76}$$

$$D = \frac{K - \text{sign}(\cos A)(1+K^2)\xi\sqrt{1-\xi^2}}{\xi^2(1+K^2)-1}. \tag{3.77}$$

Recall that ξ is given by (3.57) and v_0 is given by (2.46).

When expressing initial conditions in terms of h and A, it is simpler (and computationally more accurate) to calculate the impact parameter as

$$b = d_0 \frac{-v_0 + \cos h \sin A}{1 - v_0^2} \tag{3.78}$$

instead of using (2.43).

3.5 Initial Surface Position and Geodesic Accuracy

Section 2.7.2 described several methods for demonstrating the accuracy of the calculated geodesics. If we focus on those geodesics originating at the surface and propagating away from the star, we can survey the accuracy of the geodesics and how it is affected by their position of origin.

The calculations of emissions from neutron stars in the rest of this paper use $N_\theta = N_h = 100$. The 5th-order embedded Runge-Kutta pair is used with a tolerance of $T = 10^{-9}$. This results in 31 657 geodesics being calculated from each position on the star (except the pole which only explicitly calculates 101 geodesics). Carrying out this calculation takes 18–20 CPU-hours on an Athlon AMD 1900+ processor under the Redhat 7.3 operating system.

3.5.1 Accuracy Measured With ε^*

Figure 3.4 plots the maximum value of ε^* for each position on the surface of the star. It reveals that there are a number of pathological cases that result in higher error values than seems characteristic. These cases do not appear near the equator. For rotating stars, they otherwise appear in a seemingly random way, while they are focused near the pole for non-rotating stars. Figure 3.5 demonstrates that these aberrations are rare and few in number.

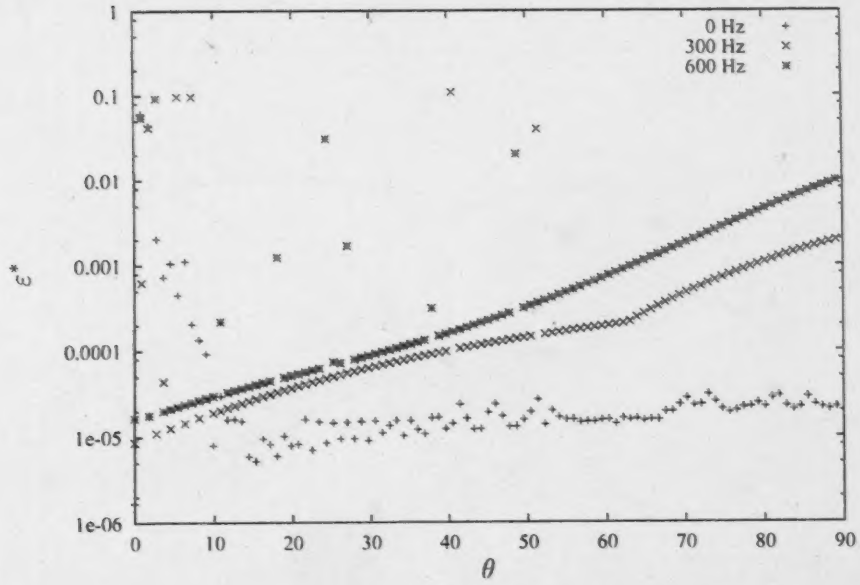

Figure 3.4: A plot of the maximum value of ε^* for each position on the star's surface vs. θ for 3 stars. The stars have equation of state eos L, mass $M = 1.4M_\odot$, and varying frequencies. This plot reveals a number of pathological cases resulting in less accuracy for some geodesics.

3.5.2 Accuracy of Geodesics from Spherical Stars

It can be shown for a non-rotating neutron star (see appendix) that the distance ℓ of the position (r, μ, ϕ) from a geodesic's plane of motion is

$$\ell = r\frac{\left|C_1(\mu_0\sqrt{1-\mu^2}\cos\phi - \sqrt{1-\mu_0^2}\mu) + C_2\sqrt{1-\mu^2}\sin\phi\right|}{\sqrt{C_1^2+C_2^2}} \quad (3.79)$$

$$C_1 = e^{(\rho_0-\gamma_0)/2}\cos h \sin A \quad (3.80)$$

$$C_2 = \varepsilon e^{-\alpha_0}\sqrt{\frac{1-\cos^2 h\sin^2 A}{1+D^2}}. \quad (3.81)$$

The angle from the plane is simply estimated from $\frac{\ell}{r}$.

The expected angle of deflection is [20]

$$\varphi = \int_0^{\frac{M}{R}} \frac{du}{\sqrt{\frac{M^2}{b^2} - (1-2u)u^2}}. \quad (3.82)$$

See section 4.5 for details on how to compute this numerically. The angle of deflection for a geodesic that started at position $(r_0, \mu_0, 0)$ and arrived at

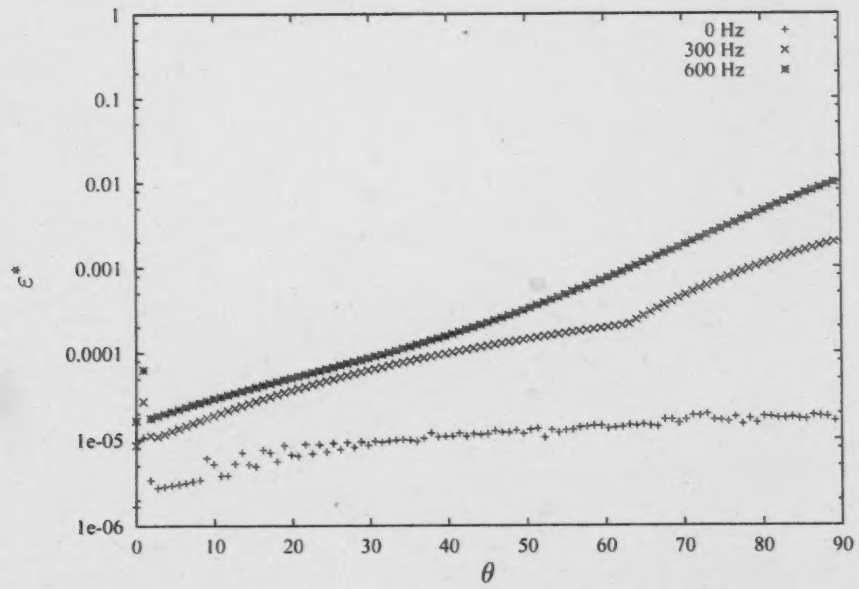

Figure 3.5: Same as in figure 3.4 except that the 3rd highest value of ε^* is plotted for each position on the star's surface. The lack of pathological cases illustrates how few they are compared to the total number of calculated geodesics.

position (r, μ, ϕ) is given by

$$\cos\varphi = \sqrt{(1-\mu_0^2)(1-\mu^2)}\cos\phi + \mu_0\mu. \tag{3.83}$$

Figure 3.6 shows the maximum values of these error estimators at each position of the star for the same non-rotating star used in figure 3.4. Except for two points near the pole, the calculated maximum angular displacement of the photons differs by about 1% from the expected maximum angle. The angular displacement in radians of the calculated geodesic from its expected plane of motion remains less than 10^{-5} for this test case.

3.5.3 Accuracy of Geodesics in the Equatorial Plane of Rotating Stars

The error estimators in this section are similar to those in the last section. Since the geodesic is in the equatorial plane, the angle from the plane is simply

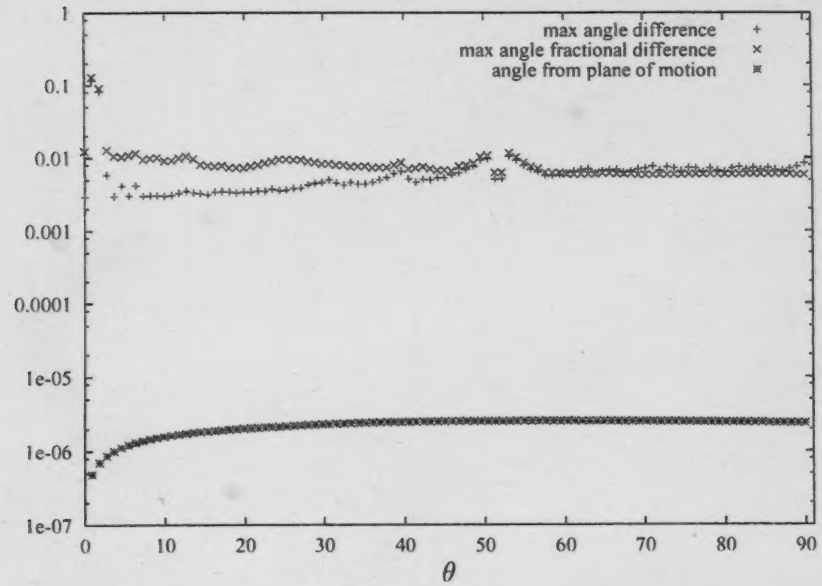

Figure 3.6: Maximum values of error estimators for non-rotating stars. The star in this calculation had equation of state eos L, mass $M = 1.4M_{\odot}$.

μ. The expected angle of deflection is found from the equations of motion.

$$\varphi = \phi = \int_{\frac{1}{2}}^{1} e^{\alpha-(\gamma+\rho)/2} \frac{\omega(1-\omega b) + e^{2\rho}\frac{b(1-s)^2}{r_e^2 s^2}}{\sqrt{(1-\omega b)^2 - e^{2\rho}\frac{b^2(1-s)^2}{r_e^2 s^2}}} \frac{r_e}{(1-s)^2} ds \tag{3.84}$$

Here, the metric potentials are evaluated at $r = \frac{r_e s}{1-s}$ and $\mu = 0$. Note that this integrand is infinite at $s = \frac{1}{2}$ when $\sin h = 0$. The angle of deflection that the numerical geodesic traveled is given by

$$\cos\varphi = \sqrt{1-\mu^2}\cos\phi. \tag{3.85}$$

Figure 3.7 shows the values of these error estimators for the star in figure 3.4 rotating at 600 Hz. The calculation is done for each altitude leaving the surface in the equatorial plane in the same direction as the star is rotating. The accuracy of counter-rotating geodesics is very similar to the co-rotating geodesics.

3.5.4 Deflection of Geodesics in the Equatorial Plane

It is interesting to note how deflection of light in the equatorial plane is affected by the star's equation of state since this determines how much of the star's

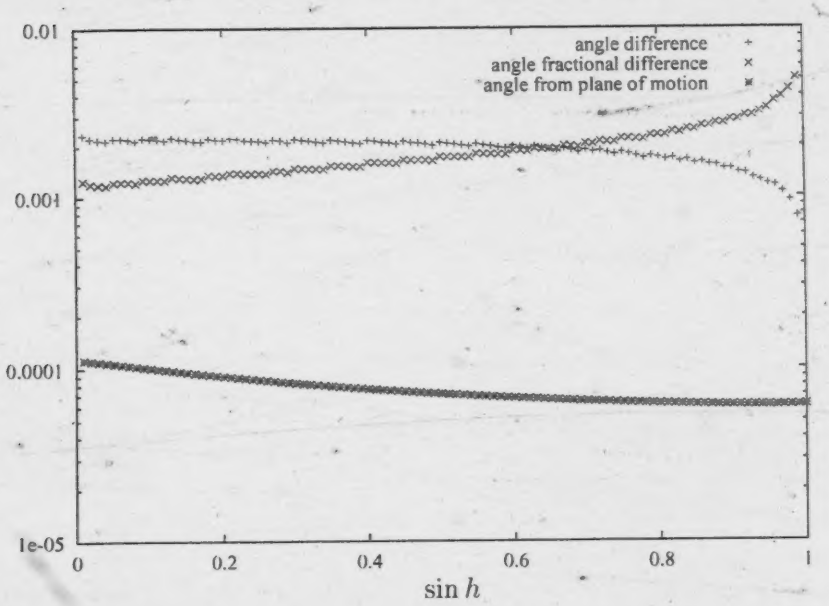

Figure 3.7: Error estimators for rotating stars. The star in this calculation had equation of state eos L, mass $M = 1.4M_{\odot}$, and frequency 600 Hz.

anterior is visible to the observer. Also, how does rotation affect how far behind the star the observer can see on both the prograde and retrograde sides of the star's equator? Figures 3.8–3.10 show the maximum deflection of light in the equatorial plane as seen by an observer in the equatorial plane. The maximum deflection is shown for both prograde (co-rotating) photons and for retrograde (counter-rotating photons). As expected, stars with larger masses produce greater angular displacements of photons. Since soft equations of state result in denser, more compact stars, It is expected that those stars would also generate larger angular displacements than stars of the same mass, but with a stiffer equation of state. This is indeed what is observed from the calculations. As a star's rotational frequency increases, retrograde photons have smaller deflections while prograde photons have deflections increase followed by, in some cases, an decrease in deflection angle as the star begins to rotate rapidly. Referring to (3.84), we can see that the decrease in prograde photon deflection angles occurs when the rotation is fast enough to have ω^2 terms be important.

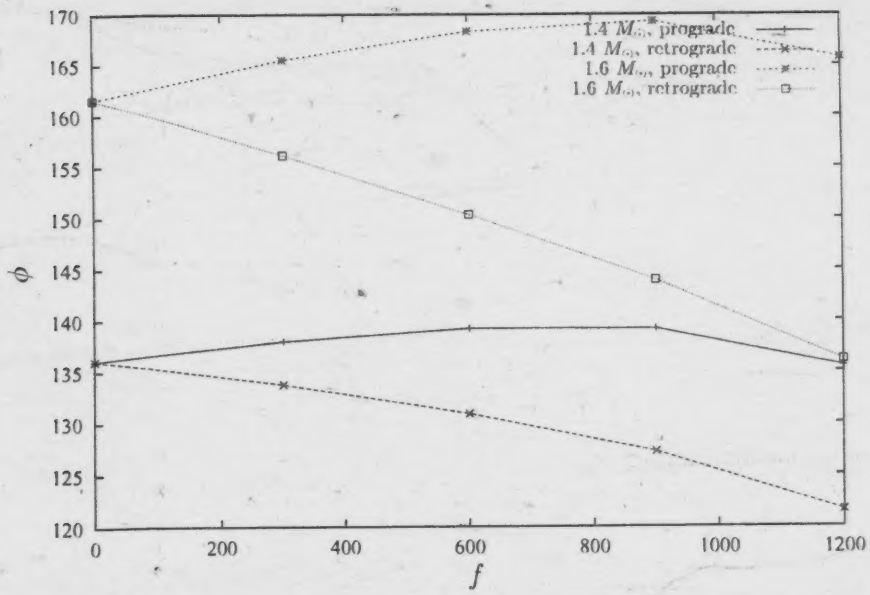

Figure 3.8: The maximum angular displacement of prograde and retrograde photons confined in the equatorial plane of stars with eos A, rotating at various frequencies.

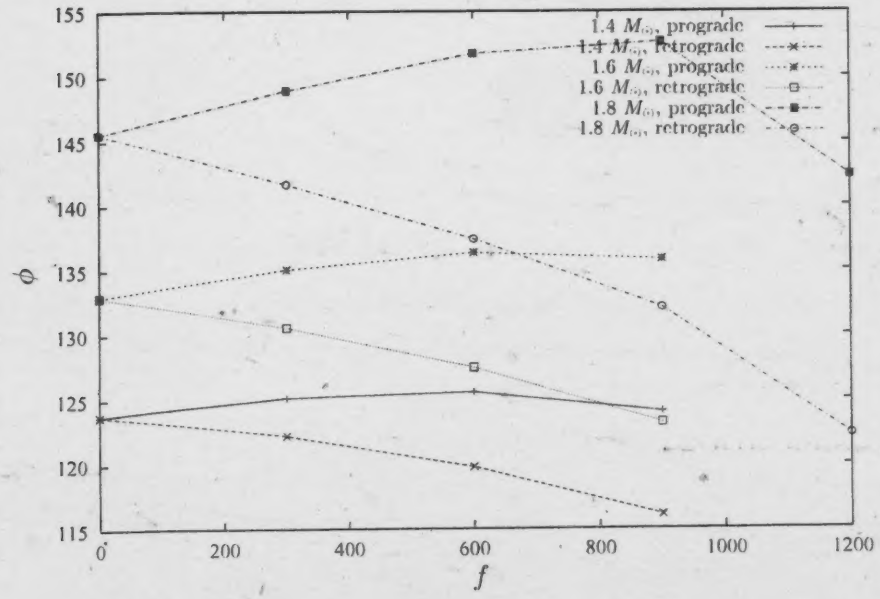

Figure 3.9: The maximum angular displacement of photons confined in the equatorial plane of stars with eos APR.

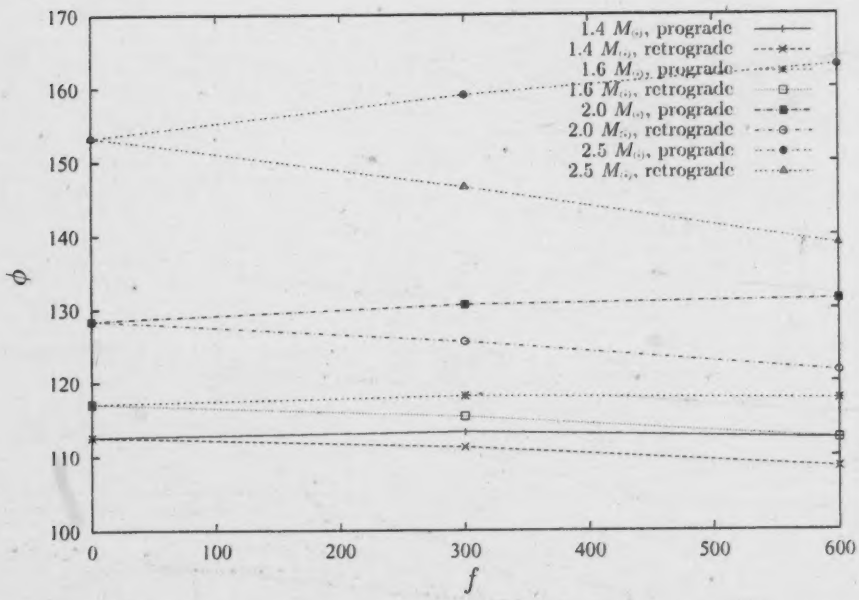

Figure 3.10: The maximum angular displacement of photons confined in the equatorial plane of stars with eos L.

Chapter 4

The Thermal Flux from Rapidly Rotating Neutron Stars

4.1 Introduction

In this chapter, we use the geometric optics approximation where light travels as rays with paths given by the geodesics of the background space-time. This approximation is valid as long as the wavelength of the light is much smaller than the radius of curvature of the space-time. A beam of radiation from a point in space is bounded by a cone generated with geodesics (see figure 4.1 for example). Such a cone forms a basis for the concept of solid angles in curved space.

Figure 4.1: In curved space-time, the value of a solid angle is different at different distances from the origin due to lensing effects. The surface of the light cone is generated by geodesics.

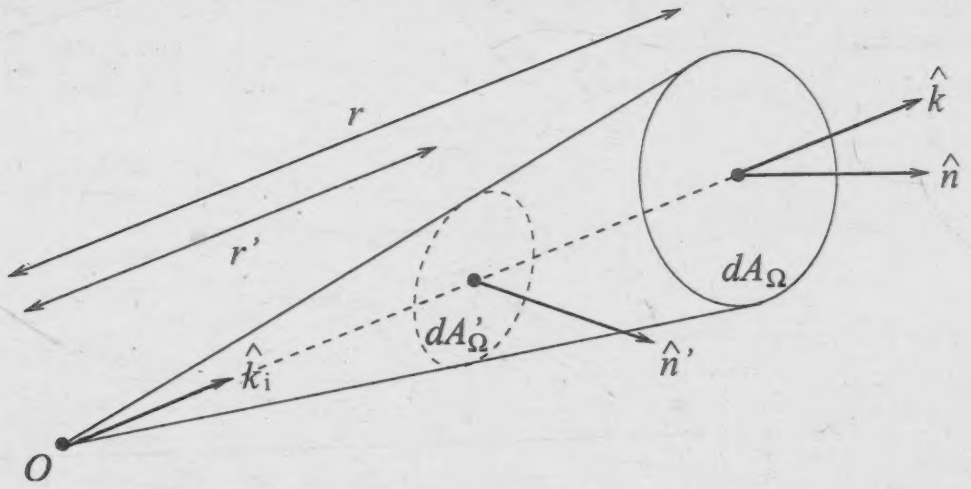

Figure 4.2: A solid angle $d\Omega$. In Cartesian space, the solid angle subtended by dA_Ω is equal to the solid angle subtended by dA'_Ω at O.

4.2 Solid Angles in Curved Space

The solid angle $d\Omega$ subtended by an area dA_Ω with unit normal $\hat{n}$ a distance r away in the $\hat{k}$ direction is (see figure 4.2) [31]

$$d\Omega = \frac{\hat{n} \cdot \hat{k}}{r^2} dA_\Omega. \tag{4.1}$$

In Cartesian space, $d\Omega$ depends only on the bounding geodesics of the area. If we choose, within the same solid angle, any other area dA'_Ω with normal $\hat{n}'$ a distance r' away, then

$$d\Omega' = \frac{\hat{n}' \cdot \hat{k}}{r'^2} dA'_\Omega = d\Omega.$$

This follows from the fact that the geodesics are straight lines within Cartesian space. This shows that as a beam of light propagates, its solid angle remains constant. Note also that $\hat{k}$ also remains constant in this case.

In curved space-time, the direction of geodesic propagation is not constant and so $\hat{k}$ is no longer constant. Also, lensing effects focus and dissipate the geodesics so that the value of the solid angle itself fluctuates and depends on the distance r from the origin O and the area subtended by the light cone at

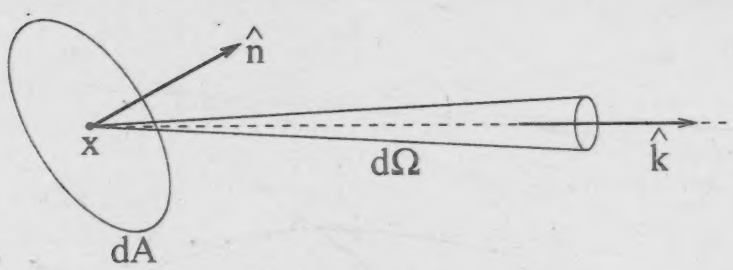

Figure 4.3: Emission of radiation.

that distance, as depicted in figure 4.1. The value of the solid angle at O is considered to be the *locally measured value* of the solid angle.

4.3 Specific Intensity and Photon Number

Let dE be the energy of radiation emitted with frequency between ν and $\nu+d\nu$ passing through an area dA that has unit normal $\hat{n}$, in time dt, emitted within a solid angle locally valued with $d\Omega$ about the direction $\hat{k}$ (see figure 4.3). Then the specific intensity $I_\nu(\hat{k}, x, t)$ is defined by [31]

$$dE = I_\nu(\hat{k}, \mathbf{x}, t)\, \hat{k} \cdot \hat{n}\, dA\, d\Omega\, d\nu\, dt. \tag{4.2}$$

Let $d\mathcal{N}$ be the number of photons in a spatial volume d^3x at position $\mathbf{x}$ with momentum volume d^3p centered at $\mathbf{p}$ at time t. Then the photon number density $n(\mathbf{x}, \mathbf{p}, t)$ in the phase space volume $d^3x d^3p$ is given by

$$d\mathcal{N} = n(\mathbf{x}, \mathbf{p}, t) d^3x d^3p. \tag{4.3}$$

Recall that photons have energy $E = h_P\nu$ and momentum $\mathbf{p} = \frac{h_P\nu}{c}\hat{k}$ where h_P is Planck's constant and c is the light speed. The energy of the radiation in the volume of phase space is

$$dE = h_P \nu n(\mathbf{x}, \mathbf{p}, t) d^3x d^3p. \tag{4.4}$$

Rewriting the phase space volume with

$$\begin{aligned} d^3x &= dx\, dA\, \hat{n} \cdot \hat{k} = c dt\, dA\, \hat{n} \cdot \hat{k} \\ d^3p &= \mathbf{p}^2 d\Omega\, dp = \left(\frac{h_P\nu}{c}\right)^2 d\Omega \left(\frac{h_P}{c}\right) d\nu = \left(\frac{h_P}{c}\right)^3 \nu^2 d\Omega d\nu \end{aligned}$$

then the energy is

$$dE = \frac{h_P^4 \nu^3}{c^2} n(\mathbf{x}, \mathbf{p}, t) \hat{n} \cdot \hat{k} dA \, d\Omega \, d\nu \, dt. \tag{4.5}$$

Comparing with (4.2), we see that the specific intensity of radiation is related to its photon number density by [31]

$$I_\nu(\hat{k}, \mathbf{x}, t) = \frac{h_P^4 \nu^3}{c^2} n(\mathbf{x}, \mathbf{p}, t). \tag{4.6}$$

Since n is an invariant, then it follows that $\frac{I_\nu}{\nu^3}$ is invariant and kept constant within a solid angle of a propagating wave front,

$$I_{\nu'}(\mathbf{x}', \mathbf{p}', t') = \left(\frac{\nu'}{\nu}\right)^3 I_\nu(\mathbf{x}, \mathbf{p}, t). \tag{4.7}$$

This result holds both in flat and curved space [20].

The photon number for blackbody emission is given by Planck's formula. So we know that the specific intensity for a blackbody of surface temperature T_0 is

$$I_\nu = \frac{2h_P}{c^2} \frac{\nu^3}{e^{h_P \nu / k_B T_0} - 1} \tag{4.8}$$

where k_B is Boltzmann's constant.

4.4 The Flux from a Neutron Star Received by a Telescope Far from the Star

Consider blackbody radiation at frequency between ν and $\nu + d\nu$ emitted from a small crossection dA of the surface of a star at altitude h from the surface in time dt. The light reaches a telescope a large distance d_s from the star with detector area dA'(see figure 4.4). If the frequency of the radiation at the telescope ranges from ν' to $\nu' + d\nu'$ and it passes through the telescope in time dt', then from (4.2) the energy received by the telescope is

$$dE' = I_\nu dA' \, d\Omega' \, d\nu' \, dt' \tag{4.9}$$

where $d\Omega'$ is the locally measured value (from the position of the telescope) of the solid angle subtended by dA at the neutron star. Because of geodesic deviation, the observer will see dA as larger than it is. That is,

$$d\Omega' = f \hat{n} \cdot \hat{k} \frac{dA}{d_s^2}$$

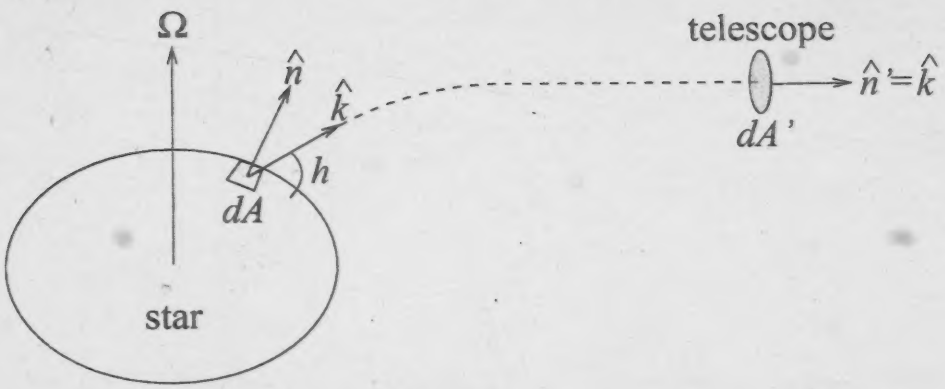

Figure 4.4: The radiation emitted from a star rotating with angular velocity Ω. The radiation is emitted from dA at an altitude h from the surface so that it reaches the telescope with area dA' far from the star.

where f acts as a magnification factor. In this work, this effect is neglected and the solid angle seen by the observer is approximated to be

$$d\Omega' \simeq \hat{n}\cdot\hat{k}\frac{dA}{d_s^2}.$$

So the flux passing through the telescope is

$$\begin{aligned} dF' &= \frac{dE'}{dA'dt'} = I_{\nu'}d\nu' d\Omega' \\ &\simeq \left(\frac{\nu'}{\nu}\right)^3 I_\nu\left(\frac{\nu'}{\nu}d\nu\right)\left(\hat{n}\cdot\hat{k}\frac{dA}{d_s^2}\right) \\ &= \frac{2h_P}{c^2}\left(\frac{\nu'}{\nu}\right)^4 \frac{\sin h}{d_s^2}\frac{\nu^3}{e^{h_P\nu/k_BT_0}-1}d\nu dA. \end{aligned} \tag{4.10}$$

The surface element on the star is

$$dA = \sqrt{2h}\,d\mu\,d\phi \tag{4.11}$$

where the 2-metric is found by considering the spacelike 3-metric perpendicular to the frame co-rotating with the star on its surface given by

$$h_{ab} = g_{ab} + u_a u_b$$

where u^a is the 4-velocity of the stellar fluid. To make this into a 3-metric, the three independent coordinates are dr, $d\mu$, and $d\phi' = d\phi - \Omega dt$. The 2-metric

is then the 3-metric constrained to the star's surface manifold. With $r_s(\mu)$ describing the surface of the star and recalling v_Ω given by (2.9), we have

$$\begin{aligned} ds_2^2 &= {}^2h_{ab}dx^a dx^b \\ &= e^{2\alpha}\left[\left(\frac{dr_s}{d\mu}\right)^2 + \frac{r_s^2}{1-\mu^2}\right]d\mu^2 + \frac{e^{\gamma-\rho}r_s^2(1-\mu^2)}{1-v_\Omega^2}d\phi'^2 \\ \Longrightarrow {}^2h &= e^{2\alpha+\gamma-\rho}\left[\left(\frac{dr_s}{d\mu}\right)^2 + \frac{r_s^2}{1-\mu^2}\right]\frac{r_s^2(1-\mu^2)}{1-v_\Omega^2} \\ &= \frac{e^{2\alpha+\gamma-\rho}(1+K^2)r_s^4}{1-v_\Omega^2} \end{aligned}$$

using (3.2). So

$$dA = e^{\alpha+(\gamma-\rho)/2}\sqrt{\frac{1+K^2}{1-v_\Omega^2}}r_s^2 d\mu d\phi'. \tag{4.12}$$

The frequency shift $\frac{\nu'}{\nu}$ is due to Doppler, gravitational redshift, and frame dragging effects. In order to calculate the change in a photon's frequency as it travels from the star to the telescope, we need to calculate the photon's energy as measured by different observers. One observer is on the star's surface and is at rest with respect to the rotating star. The other observer is at the telescope. Given an observer with 4-velocity u^a, the energy of the photon with 4-momentum p_a measured by the observer is E_u given by (see [29], for example)

$$E_u = -p_a u^a.$$

The photon frequency measured by the observer is then

$$\nu_u = \frac{E_u}{h_P}.$$

Consider a photon emitted from the surface of a rotating neutron star with impact parameter b. Then its 4-momentum is given by (2.12). An observer located at dA on the star's surface, co-rotating with the star has 4-velocity given by (2.7). So the frequency of the emitted photon measured by the observer is

$$\nu_0 = -p_a u^a = \frac{E}{h_P}e^{-(\gamma_0+\rho_0)/2}\frac{1-\Omega b}{\sqrt{1-v_\Omega^2}}. \tag{4.13}$$

An inertial observer far from the star has 4-velocity $u^a_\infty = t^a$, so

$$\nu_\infty = -p_a t^a = \frac{E}{h_P}. \tag{4.14}$$

(Recall that this is the definition of E). So the total shift in frequency of a photon from the star's surface to the telescope is

$$\frac{\nu_\infty}{\nu_0} = e^{(\gamma_0+\rho_0)/2}\frac{\sqrt{1-v_\Omega^2}}{1-\Omega b}. \tag{4.15}$$

In the limit of a non-rotating star $v_\Omega = \Omega = 0$ and

$$\lim_{\Omega\to 0}\frac{\nu_\infty}{\nu_0} = e^{(\gamma_0+\rho_0)/2} = \sqrt{1-\frac{2M}{R}}$$

which is the standard gravitational redshift effect for a spherical body. In the absence of the frame-dragging term ω, and for photons emitted with extreme values of b given by (3.13), the quantity $\frac{\sqrt{1-v_\Omega^2}}{1-\Omega b}$ reduces to

$$\sqrt{\frac{1\mp\Omega d}{1\pm\Omega d}},$$

the standard Doppler shift term (where the upper sign corresponds to the fluid moving away from us and the lower sign corresponds to fluid moving toward us).

So in all, the flux received by the telescope from the star is

$$F = \frac{2h_P}{c^2 d_s^2}\int_0^\infty\int_{-1}^1\int_0^{2\pi} e^{\alpha+(5\gamma+3\rho)/2}\frac{(1-v_\Omega^2)^2\sin h}{(1-\Omega b)^4} \frac{\nu_0^3}{e^{h_P\nu_0/k_BT_0}-1}\sqrt{\frac{1+K^2}{1-v_\Omega^2}}r_s^2 d\phi d\mu d\nu_0 \tag{4.16}$$

where $b(\mu,\phi)$ and $h(\mu,\phi)$ here are respectively the impact parameter and altitude of a photon originating at the (μ,ϕ) position on the star's surface and reaching the position of the telescope. Since

$$\int_0^\infty \frac{\nu_0^3}{e^{h_P\nu_0/k_BT_0}-1}d\nu_0 = \frac{1}{15}\left(\frac{\pi k_B T_0}{h_P}\right)^4$$

then

$$F = \frac{2\pi^4}{15}\frac{(k_BT_0)^4}{c^2h_P^3d_s^2}\int_{-1}^1 e^{\alpha+(5\gamma+3\rho)/2}\sqrt{(1+K^2)(1-v_\Omega^2)^3}\,r_s^2\int_0^{2\pi}\frac{\sin h}{(1-\Omega b)^4}d\phi\,d\mu. \tag{4.17}$$

Rather than calculate F, it is more convenient to calculate the dimensionless quantity

$$\begin{aligned} \mathcal{F} &\equiv \frac{h_P^3 c^2}{\kappa} \frac{4\pi d_s^2 F}{(k_B T_0)^4} \\ &= \frac{8\pi^5}{15} \int_{-1}^{1} e^{\alpha+(5\gamma+3\rho)/2} \sqrt{(1+K^2)(1-v_\Omega^2)^3}\, \frac{r_s^2}{\kappa} \int_0^{2\pi} \frac{\sin h}{(1-\Omega b)^4} d\phi\, d\mu \end{aligned} \tag{4.18}$$

where κ, given by (2.41), gives us a fundamental length scale of the system. We can use $\mathcal{F}$ to compare the flux received from equidistant neutron stars at the same temperature since then $\frac{F_1}{F_2} = \frac{\mathcal{F}_1}{\mathcal{F}_2}$.

4.5 The Flux Received from a Spherical Neutron Star

4.5.1 The Spherical Limit of the Calculated Flux

It is useful to be able to calculate the flux due to a spherical neutron star to test the accuracy of the rotating flux code for the non-rotating case.

The expressions in this section are most easily written using the Schwarzschild radial coordinate instead of the isotropic coordinate. In this section, I will write the radius of the star in isotropic coordinates as $\overline{R}$, and simply as R in the Schwarzschild coordinate system. They are related by

$$R = \overline{R}\left(1 + \frac{M}{2\overline{R}}\right)^2 \tag{4.19}$$

where M is the mass of the star in geometric units.

For a non-rotating star, we have $\Omega = 0$ giving $v_\Omega = 0$, $K = 0$ since the star is spherical, and the radius of the star being $r_s = \overline{R}$. Referring to equations (2.3)-(2.5), the values of the metric potentials on the surface of the star are given by

$$e^{(\gamma_0-\rho_0)/2} = e_0^\alpha = \left(1 + \frac{M}{2\overline{R}}\right)^2 = \frac{R}{\overline{R}} \tag{4.20}$$

$$e^{(\gamma_0+\rho_0)/2} = \frac{1-\frac{M}{2\overline{R}}}{1+\frac{M}{2\overline{R}}} = \sqrt{1-\frac{2M}{R}} \tag{4.21}$$

$$\omega_0 = 0. \tag{4.22}$$

Then the dimensionless flux of a spherical star received by a telescope far from the star is

$$\mathcal{F}_{\text{sph}} = \frac{8\pi^5}{15}\frac{R^2}{\kappa}\left(1-\frac{2M}{R}\right)^2 \int \sin h \, dA \tag{4.23}$$

integrated over the surface of the star that is visible to the telescope where h is the altitude of the photons that reach the telescope from each position on the surface of the star. Because of spherical symmetry, the altitude h of the photon that reaches the observer depends only on the total angle of deflection φ of the photon path.

$$\mathcal{F}_{\text{sph}} = \frac{16\pi^6}{15}\frac{R^2}{\kappa}\left(1-\frac{2M}{R}\right)^2 \int_0^{\varphi_{\max}} \sin\varphi \sin h(\varphi) d\varphi \tag{4.24}$$

Because of spherical symmetry, we can assume that the telescope is on the x-axis ($\mu = \phi = 0$). Then the deflection of the photon originating on the surface of the star at μ_0 and ϕ_0 that reaches the telescope is

$$\cos\varphi = \sqrt{1-\mu^2}\cos\phi. \tag{4.25}$$

Referring to (2.31), the ϕ evolution of a geodesic at the surface of a spherical neutron star is $\dot{\phi}_0 = \frac{b}{R^2(1-\mu^2)}$. So the spherical limit of (3.30) is

$$\sin h = \sqrt{\left[1-\left(1-\frac{2M}{R}\right)\frac{b^2}{R^2}\right]\frac{1}{1+\frac{1}{D^2}}}. \tag{4.26}$$

By carrying out the integration over φ in the equatorial plane of the star, then $\frac{1}{D} = 0$.

$$\cos h = \sqrt{1-\frac{2M}{R}}\frac{b}{R} \tag{4.27}$$

When a photon is constrained to propagate in the equator of the star, its deflection is [20]

$$\varphi = \int_0^{\frac{M}{R}} \frac{du}{\sqrt{\frac{M^2}{b^2}-(1-2u)u^2}} \tag{4.28}$$

where $u = \frac{M}{r}$ and r is the Schwarzschild radial coordinate. For photons not in the equatorial plane, the altitude must have the same value as for a photon

in the equatorial plane with the same deflection from the telescope. So in general,

$$\cos h = \sqrt{1 - \frac{2M}{R}}\frac{b_\phi}{R} \tag{4.29}$$

where b_ϕ is the impact parameter of a photon in the equatorial plane with the required angular deflection φ.

To see the relationship between b and b_ϕ, substitute (4.29) into the spherical limit of (3.78)

$$b = \frac{R\sqrt{1-\mu_0^2}}{\sqrt{1-\frac{2M}{R}}}\cos h \sin A \tag{4.30}$$

giving us

$$b = b_\phi\sqrt{1-\mu_0^2}\sin A. \tag{4.31}$$

In summary, the flux of a non-rotating neutron star seen by an observer is calculated by

$$\mathcal{F}_{\text{sph}} = \frac{16\pi^6}{15}\frac{R^2}{\kappa}\left(1-\frac{2M}{R}\right)^2\int_0^{\varphi_{\max}}\sqrt{1-\left(1-\frac{2M}{R}\right)\frac{b_\phi^2(\varphi)}{R^2}}\sin\varphi\, d\varphi \tag{4.32}$$

where $b_\phi(\varphi)$ satisfies

$$\varphi = \int_0^{\frac{M}{R}} \frac{du}{\sqrt{\frac{M^2}{b_\phi^2} - (1-2u)u^2}}. \tag{4.33}$$

The maximum angle of deflection $\varphi_{\max}$ is determined by the maximum impact parameter $b_{\phi_{\max}}$, constrained by requiring

$$\frac{M^2}{b_\phi^2} \geq (1-2u)u^2$$

for $0 < u \leq \frac{M}{R}$ (see figure 4.5).

$$b_{\phi_{\max}} = \max_{0<u\leq\frac{M}{R}} \frac{M}{u\sqrt{1-2u}} = \begin{cases} \frac{R}{\sqrt{1-\frac{2M}{R}}}, & 0 < \frac{M}{R} \leq \frac{1}{3} \\ \sqrt{27}M, & \frac{1}{3} < \frac{M}{R} < \frac{1}{2} \end{cases} \tag{4.34}$$

Numerically evaluating (4.33) can be problematic as the integrand is singular when $b_\phi = b_{\phi_{\max}}$ and $u = \min\left(\frac{M}{R}, \frac{1}{3}\right)$. However, by noting that the integral is elliptic, the integration may be rewritten in terms of elliptic functions. To do this, we begin by factoring the radicand in the integral:

$$u_b^2 - (1-2u)u^2 = 2(u-a_1)(u-a_+)(u-a_-) \tag{4.35}$$

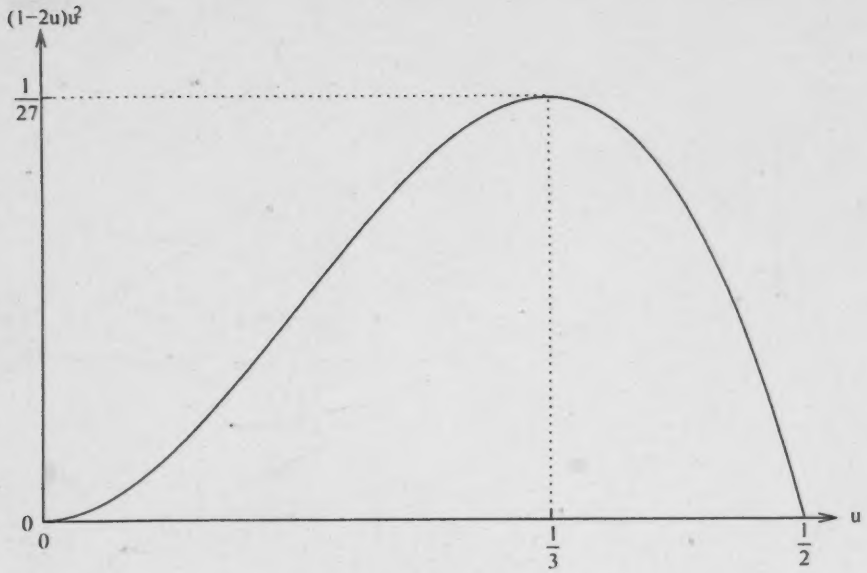

Figure 4.5: A plot of $f(u) = (1-2u)u^2$.

where

$$\begin{aligned} u_b &= \frac{M}{b_\phi}, \\ a_1 &= \frac{1}{6}\left(1 + C + \frac{1}{C}\right), \\ a_\pm &= -\frac{1}{12}\left[C + \frac{1}{C} - 2 \pm i\sqrt{3}\left(C - \frac{1}{C}\right)\right], \\ C^3 &= 1 - 54u_b^2\left(1 - \sqrt{1 - \frac{1}{27u_b^2}}\right). \end{aligned}$$

See figure 4.6 for a plot of the roots. There are two main cases to consider: $u_b^2 > \frac{1}{27}$ and $u_b^2 < \frac{1}{27}$.

Case 1: $u_b^2 > \frac{1}{27}$

From (4.34), it follows that all geodesics from stars with $\frac{M}{R} > \frac{1}{3}$ are of this case.

The value of C is real-valued in this case, and so a_1 is real and $a_\pm$ are complex. Since $C^2 + C + 1 > 0$ for all real values of C, there is no real value of C for which $a_1 = 0$. Also, $a_1 = -\frac{1}{6} < 0$ when $u_b = \frac{1}{\sqrt{27}}$. So continuity of a_1 when C is real implies that $a_1 < 0$ in this range. Then the integration

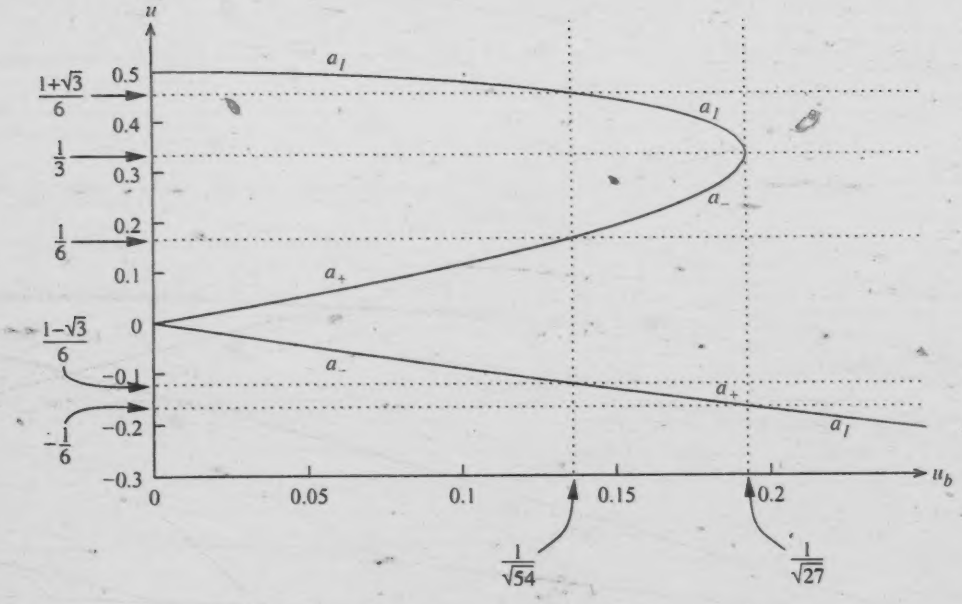

Figure 4.6: The roots of $u_b^2 - (1-2u)u^2$.

domain of (4.33) is within the interval $u > a_1$. Then by referring to Byrd and Friedman's Handbook for Elliptic Integrals [7], page 86, then (4.33) can be rewritten as

$$\begin{aligned}
\varphi &= \frac{1}{\sqrt{2}}\left[\int_{a_1}^{\frac{M}{R}} \frac{du}{\sqrt{(u-a_1)[(u-b_1)^2+c_1^2]}} - \int_{a_1}^{0} \frac{du}{\sqrt{(u-a_1)[(u-b_1)^2+c_1^2]}}\right] \\
&= g[F(\varphi_1,k) - F(\varphi_0,k)] \\
&= g\left[\int_0^{y_1} \frac{dt}{\sqrt{(1-t^2)(1-k^2t^2)}} - \int_0^{y_0} \frac{dt}{\sqrt{(1-t^2)(1-k^2t^2)}}\right] \\
&= g\int_{y_0}^{y_1} \frac{dt}{\sqrt{(1-t^2)(1-k^2t^2)}} \qquad (4.36)
\end{aligned}$$

where

$$\begin{aligned}
b_1 &= \frac{1}{12}\left(2 - C - \frac{1}{C}\right) \\
c_1 &= \frac{\sqrt{3}}{12}\left(C - \frac{1}{C}\right) \\
A^2 &= (b_1 - a_1)^2 + c_1^2 = \frac{1}{12}\left(1 + C^2 + \frac{1}{C^2}\right) \\
g &= \frac{1}{\sqrt{2A}}
\end{aligned}$$

$$
\begin{aligned}
y_0 &= \sin\varphi_0 = \frac{2\sqrt{-Aa_1}}{A-a_1} \\
y_1 &= \sin\varphi_1 = \frac{2\sqrt{A\left(\frac{M}{R}-a_1\right)}}{A-a_1+\frac{M}{R}} \\
k^2 &= \frac{1}{2}\left(1+\frac{b_1-a_1}{A}\right) = \frac{1}{2}\left(1+\frac{1}{\sqrt{1+\frac{1}{3}\left(\frac{1-C^2}{1+C^2}\right)^2}}\right)
\end{aligned}
$$

and

$$
F(\varphi,k) \equiv \int_0^{\varphi} \frac{d\theta}{\sqrt{1-k^2\sin^2\theta}}
$$

is the elliptic integral of the first kind. Numerically evaluating (4.36) is much simpler than (4.33).

Case 2: $u_b^2 < \frac{1}{27}$

As was argued in case 1, we must have $\frac{M}{R} \leq \frac{1}{3}$ in this case. For this range of u_b, C is complex and we end up with 3 real roots. Separate C into real and imaginary parts by writing $C = C_r + iC_i = |C|e^{iC_\phi}$ where C_r, C_i, $|C|$, and C_ϕ are real numbers. Since

$$
C^3 = 1 - 54u_b^2 + i54u_b^2\sqrt{\frac{1}{27u_b^2}-1}
$$

then

$$
\begin{aligned}
|C|^3 = \sqrt{(1-54u_b^2)^2 + \left(54u_b^2\sqrt{\frac{1}{27u_b^2}-1}\right)^2} &= 1 \\
\implies |C| &= 1 \qquad (4.37)
\end{aligned}
$$

and

$$
\begin{aligned}
3C_\phi &= \tan^{-1}\left(\frac{54u_b^2\sqrt{\frac{1}{27u_b^2}-1}}{1-54u_b^2}\right) \\
&= \tan^{-1}\left(\frac{\sqrt{1-(1-54u_b^2)^2}}{1-54u_b^2}\right) \\
&= \text{sign}(54u_b^2-1)\cos^{-1}(1-54u_b^2). \qquad (4.38)
\end{aligned}
$$

The roots are then

$$\begin{aligned} a_1 &= \frac{1}{6}\left[1 + (C_r + iC_i) + \frac{C_r - iC_i}{|C|^2}\right] \\ &= \frac{1}{6}(1 + 2C_r) \\ &= \frac{1}{6}\left[1 + 2\cos\left(\frac{1}{3}\cos^{-1}(1 - 54u_b^2)\right)\right] \end{aligned} \tag{4.39}$$

$$\begin{aligned} a_\pm &= \frac{1}{12}(2 - 2C_r \pm 2\sqrt{3}C_i) \\ &= \frac{1}{6}\left[1 - \cos\left(\frac{1}{3}\cos^{-1}(1 - 54u_b^2)\right)\right. \\ &\quad \left. \pm \operatorname{sign}(54u_b^2 - 1)\sqrt{3}\sin\left(\frac{1}{3}\cos^{-1}(1 - 54u_b^2)\right)\right]. \end{aligned} \tag{4.40}$$

Note that

$$\cos x \pm \sqrt{3}\sin x = 2\cos\frac{\pi}{3}\cos x \pm 2\sin\frac{\pi}{3}\sin x = 2\cos\left(\frac{\pi}{3} \mp x\right)$$

and relabel the roots as

$$a_2 = \frac{1}{6}\left[1 - 2\cos\left(\frac{\pi}{3} + \frac{1}{3}\cos^{-1}(1 - 54u_b^2)\right)\right] \tag{4.41}$$

$$a_3 = \frac{1}{6}\left[1 - 2\cos\left(\frac{\pi}{3} - \frac{1}{3}\cos^{-1}(1 - 54u_b^2)\right)\right]. \tag{4.42}$$

Then $a_1 > a_2 \geq 0 \geq a_3$.

In order for the integrand of (4.33) to be real over the range of integration, we require $\frac{M}{R} \leq a_2$. Our original criteria for a real integrand was $u_b^2 \geq \left(\frac{M}{R}\right)^2\left(1 - \frac{2M}{R}\right)$. To see that these criteria are equivalent:

$$\begin{aligned} & \frac{M}{R} \leq a_2 = \frac{1}{6}\left[1 - 2\cos\left(\frac{\pi}{3} + \frac{1}{3}\cos^{-1}(1 - 54u_b^2)\right)\right] \\ \Longrightarrow \quad & \cos\left(\frac{\pi}{3} + \frac{1}{3}\cos^{-1}(1 - 54u_b^2)\right) \leq \frac{1}{2}\left(1 - \frac{6M}{R}\right) \\ \Longrightarrow \quad & \frac{\pi}{3} + \frac{1}{3}\cos^{-1}(1 - 54u_b^2) \geq \cos^{-1}\left(\frac{1}{2} - \frac{3M}{R}\right) \end{aligned}$$

where the facts $u_b^2 < \frac{1}{27}$ and $\frac{M}{R} \leq \frac{1}{3}$ were used. Then

$$\begin{aligned} 1 - 54u_b^2 &\leq \cos\left(3\cos^{-1}\left(\frac{1}{2} - \frac{3M}{R}\right) - \pi\right) \\ &= -\cos\left(3\cos^{-1}\left(\frac{1}{2} - \frac{3M}{R}\right)\right) \\ &= -4\left(\frac{1}{2} - \frac{3M}{R}\right)^3 + 3\left(\frac{1}{2} - \frac{3M}{R}\right) \\ &= 108\left(\frac{M}{R}\right)^3 - 54\left(\frac{M}{R}\right)^2 + 1 \\ \Longrightarrow\ u_b^2 &\geq \left(\frac{M}{R}\right)^2\left(1 - \frac{2M}{R}\right) \end{aligned}$$

meeting our expectations. The third line used the identity

$$\cos(3x) = 4\cos^3 x - 3\cos x.$$

The domain of the integration of (4.33) is therefore $a_3 < 0 \leq u \leq \frac{M}{R} \leq a_2$. Referring to page 74 of Byrd and Friedman [7], (4.33) is written as

$$\begin{aligned} \varphi &= \frac{1}{\sqrt{2}}\left[\int_0^{a_2} \frac{du}{\sqrt{(u-a_1)(u-a_2)(u-a_3)}} \right. \\ &\qquad \left. - \int_{\frac{M}{R}}^{a_2} \frac{du}{\sqrt{(u-a_1)(u-a_2)(u-a_3)}}\right] \\ &= g[F(\varphi_0, k) - F(\varphi_1, k)] \\ &= g\int_{y_1}^{y_0} \frac{dt}{\sqrt{(1-t^2)(1-k_1^2t^2)}} \end{aligned} \tag{4.43}$$

where

$$\begin{aligned} g &= \sqrt{\frac{2}{a_1 - a_3}} \\ k_1 &= \sqrt{\frac{a_2 - a_3}{a_1 - a_3}} \\ y_0 &= \sin\varphi_0 = \sqrt{\frac{(a_1 - a_3)a_2}{(a_2 - a_3)a_1}} \\ y_1 &= \sin\varphi_1 = \sqrt{\frac{(a_1 - a_3)(a_2 - \frac{M}{R})}{(a_2 - a_3)(a_1 - \frac{M}{R})}}. \end{aligned}$$

In summary, the flux received by a telescope given by (4.18) in the limit of a spherical star is given by (4.32), with $b_\phi(\varphi)$ determined from (4.36) or (4.43).

4.5.2 The Exact Flux of a Spherical Star

It is known that at the surface of a spherical blackbody with radius R and surface temperature T_0 , its luminosity is

$$L = 4\pi R^2 \sigma T^4 \tag{4.44}$$

where

$$\sigma = \frac{2\pi^5 k_B^4}{15 h_P^3 c^2}$$

is the Stefan-Boltzmann constant. To determine the flux of a star, we need to determine the luminosity of the star, far from the star. The metric outside the star is Schwarzschild. Following the methods of (4.13)–(4.15), the 4-velocity and 4-momentum of an observer with energy E at rest with respect to the star and at the surface of the star having mass M and radius R is

$$u^a = \frac{1}{\sqrt{1 - \frac{2M}{R}}} t^a \tag{4.45}$$

$$p_a = -E \nabla_a t. \tag{4.46}$$

Then the shift in frequency observed by the observer at the star and the observer at infinity is

$$\frac{\nu_\infty}{\nu_0} = \frac{t^a p_a}{u^b p_b} = \sqrt{1 - \frac{2M}{R}}. \tag{4.47}$$

The luminosity of the star at its surface is the sum of the energy $h_P \nu_0$ of all photons emitted from the star in unit time Δt_0. Consider the luminosity L_{ν_0} due to photons emitted with a specific frequency ν_0. Then $L_{\nu_0} = N_{\nu_0} h_P \nu_0$ where N_{ν_0} is the number of emitted photons with frequency ν_0 in time Δt_0. Define L_∞ to be the rate that energy passes through a sphere, centered at the star and with very large radius compared to the neutron star's equatorial radius. Similarly, let the luminosity at the large sphere due to those photons emitted with frequency ν_0 be denoted $L_{\nu_\infty} = N_{\nu_\infty} h_P \nu_\infty$ where ν_∞ is the frequency that ν_0 is redshifted to, and N_{ν_∞} is the number of photons received at the large sphere in unit time. Now clocks run more slowly near the star than far from it, accounting for the redshifting of the photons. Since $\Delta t \propto \nu^{-1}$, then $\frac{\Delta t_0}{\Delta t_\infty} = \frac{\nu_\infty}{\nu_0}$. If we assume that photons of each frequency are emitted at a constant rate,

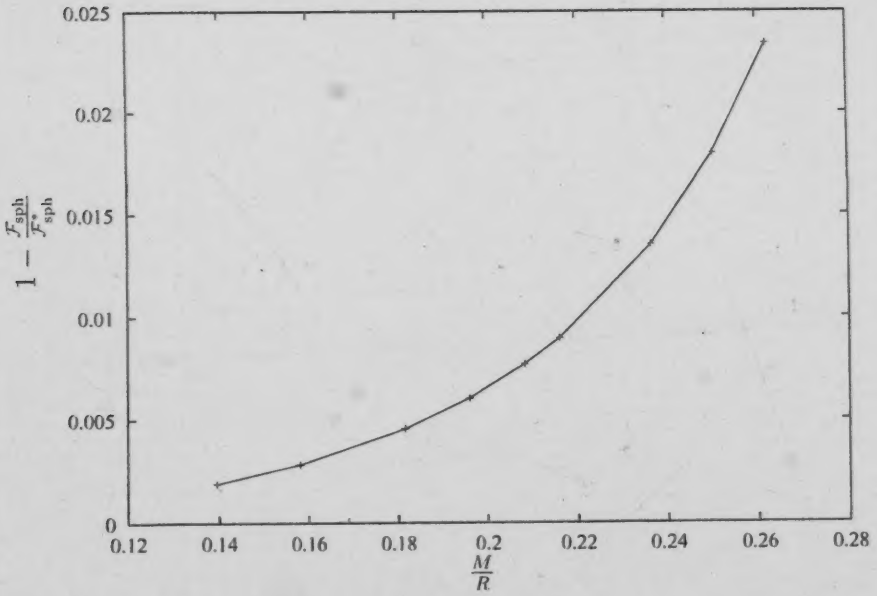

Figure 4.7: The fractional difference between $\mathcal{F}_{\rm sph}$ and $\mathcal{F}^*_{\rm sph}$ increases as $\frac{M}{R}$ increases.

then $\frac{N_{\nu_0}}{N_{\nu_\infty}} = \frac{\Delta t_0}{\Delta t_\infty}$. It then follows that $L_{\nu_\infty} = N_{\nu_0} h_P \nu_0 \left(\frac{\nu_\infty}{\nu_0}\right)^2 = L_{\nu_0}\left(1 - \frac{2M}{R}\right)$. Doing the same calculation for each emitted frequency of photon and adding all the contributions relates the star's true luminosity L to L_∞ by

$$L_\infty = L\left(1 - \frac{2M}{R}\right). \tag{4.48}$$

Then the flux of the spherical star at a distance d_s from the star is

$$F^*_{\rm sph} = \frac{L_\infty}{4\pi d_s^2} \tag{4.49}$$

and referring to (4.18) we have

$$\mathcal{F}^*_{\rm sph} = \frac{8\pi^6}{15}\frac{R^2}{\kappa}\left(1 - \frac{2M}{R}\right). \tag{4.50}$$

To see how (4.50) compares with its approximation (4.32), the spherical limit of (4.18) we plot their fractional difference against $\frac{M}{R}$ of the star (see figure 4.7). The fact that the difference increases with $\frac{M}{R}$ is in accordance with the fact that we neglected the general relativistic geodesic deviation effect. However, the error is within a few percent of the value of the flux of the star.

4.6 Calculating the Flux: Results

Assume that the observer (telescope) is located at latitude θ_{obs}. Because of azimuthal symmetry, we may choose the coordinate system such that $\phi_{\text{obs}} = 0$.

To calculate the flux from a neutron star measured by the observer, we use (4.18). This is done by first determining the functions $h(\mu_0, \phi_0)$ and $b(\mu_0, \phi_0)$, the altitude and impact parameters of the photons originating at (μ_0, ϕ_0) on the star's surface, and reach the observer's position at an infinite distance from the star. The procedure is as follows:

1. An initial position (μ_0, ϕ_0) on the star is chosen with $\phi_0 = 0$.
2. An initial altitude h is chosen.
3. All photons with these initial values are generated, and their final values of angular position (μ_f, ϕ_f) are computed.
4. The observer is located at $(\mu_{\text{obs}}, 0)$. If one of the photons generated in the last step has $\mu_f = \mu_{\text{obs}}$, then it would have hit the detector if it had initial conditions $(\mu_0, -\phi_f)$.

In this way, we determine the initial positions, altitudes, and impact parameters of all the photons that hit the detector. Note that more than one photon from each location and altitude could hit the detector. See figure 4.8 for samples of the results of this calculation. In this figure, each value of altitude occurs for at most two longitudes for each latitude of the star. Neutron stars for which this is not the case are not yet supported by this program. Sometimes, small errors in the final positions of the geodesics will result in "blips". These occur when the final position of a geodesic is displaced enough that a particular latitude has more than 2 values of longitude (see figure 4.9). Such occurrences are easily detected, but are currently not handled by the code; detection of a blip causes the calculation of flux to fail. Fortunately, blips are relatively rare and can normally be sidestepped by a small adjustment of the observer's position in the star's sky.

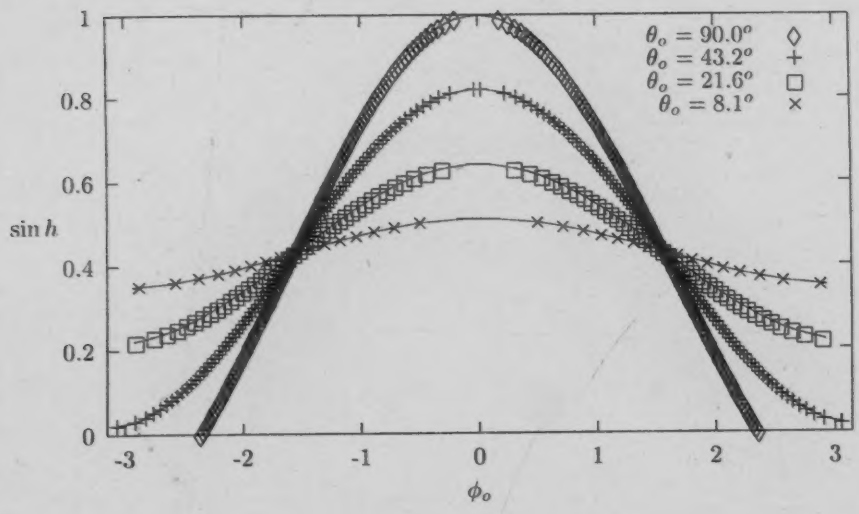

Figure 4.8: Constructed functions $\sin h(\phi)$ for various initial latitudes on a spherical star of mass $M = 1.4M_\odot$ and equation of state A where the observer is located in the star's equatorial plane. The points are the calculated values of the function from the emission of the neutron star, and the lines cover the theoretical values determined from solving (4.33) and (4.29) for h given the appropriate angular displacement φ. The curves cross at $\phi_0 = \frac{\pi}{2}$ where they take the value of the altitude of the photon reaching the observer from the star's poles.

Figure 4.10 compares the methods for calculating the flux of a non-rotating neutron star measured by an observer far from the star. In every case except for the eos APR star of mass $2.0M_\odot$, the values of $\mathcal{F}$ and $\mathcal{F}_{\text{sph}}$ are within 1%.

Figure 4.11 plots the fractional difference between the maximum angle of deflection of photons leaving the surface of a spherical neutron star as determined from the emission of the neutron star, and calculated theoretically from (4.33). In all cases, they are within 1%.

To see how the code works for observers located at different latitudes, we plot the observed flux versus the latitude of the observer for a non-rotating star and compare the result to the theoretical value $\mathcal{F}_{\text{sph}}$ (see figure 4.12).

We can see that our method works best when closer to the equator and completely fails at the pole of the star. To see why this is, consider the observer at the pole's position $\mu_{\text{obs}} = 1$. Since this is the maximal value of μ,

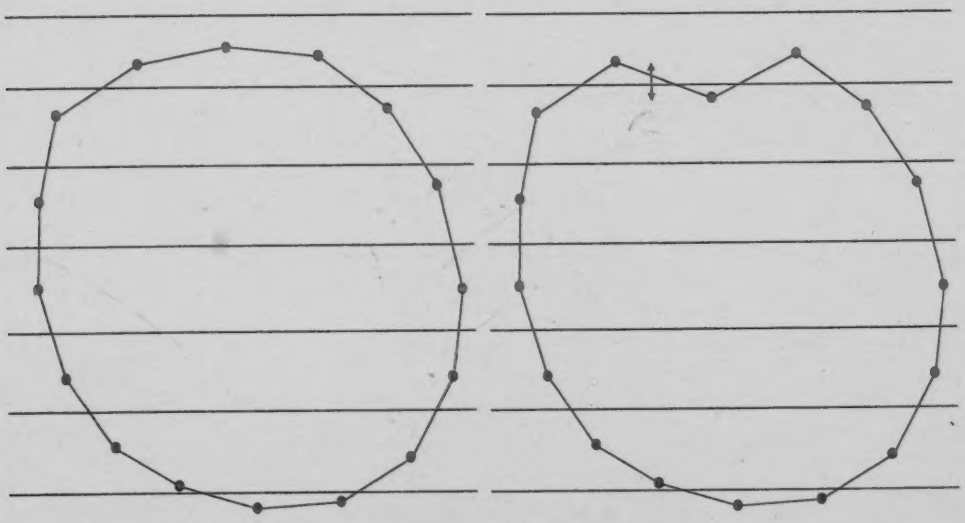

Figure 4.9: This figure represents the star's sky. The points are final destinations of a set of photons all propagating with the same altitude from one position on the star's surface. The horizontal lines represent lines of constant latitude in the star's sky. It is expected that the photons should follow a pattern similar to the left diagram where each latitude has at most two geodesics reach it. The right diagram contains an example of a "blip" where one of the points is misplaced due to numerical error in such a way that an interval of latitudes (shown by the vertical arrow) have more than two geodesics reach it.

it will be missed by all interpolations between subsequent latitudes of photon destinations unless a photon should just happen to reach the z-axis exactly, a rare event indeed. Hence, practically all contributions to the flux measured by the observer is missed in this case. This effect becomes less of a problem the further the observer is from the pole. Figure 4.13 shows the flux profile for the same star rotating at a frequency of 600 Hz. Based on the results for the spherical star, it is expected that this profile is most accurate near the equator and is completely wrong near the pole.

The fractional increase in flux of a neutron star of a given mass (measured by an observer in the star's equatorial plane) as its frequency increases is shown in figure 4.14 where $\mathcal{F}_0$ represents the calculated flux measured for the non-rotating model. At 600 Hz, the increase in brightness of stars with eos L is significantly more than for the stars with eos A or eos APR. At higher spin frequencies, the fractional increase in brightness for stars with eos APR become

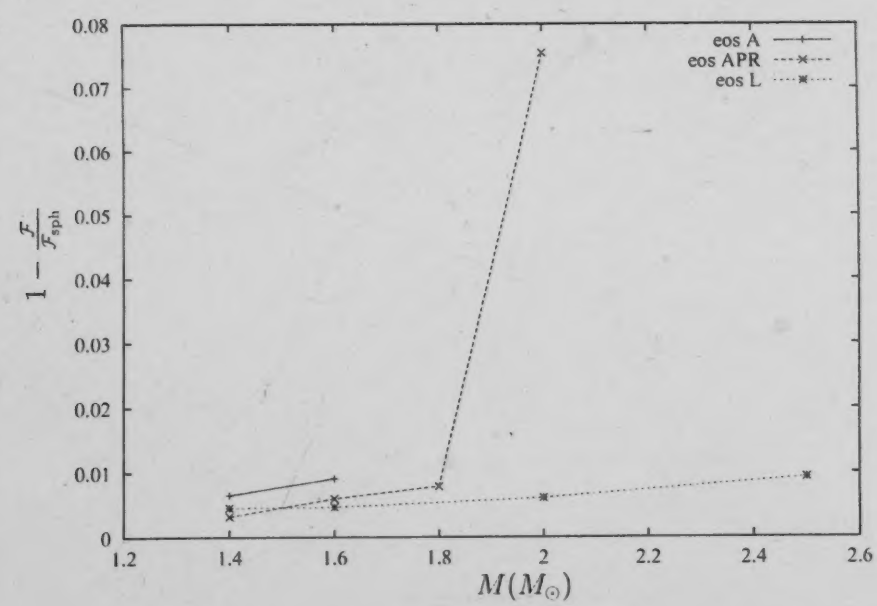

Figure 4.10: The fractional difference between $\mathcal{F}$ and $\mathcal{F}_{\rm sph}$ for all calculated spherical models where $\mathcal{F}$ is calculated with the observer in the star's equatorial plane.

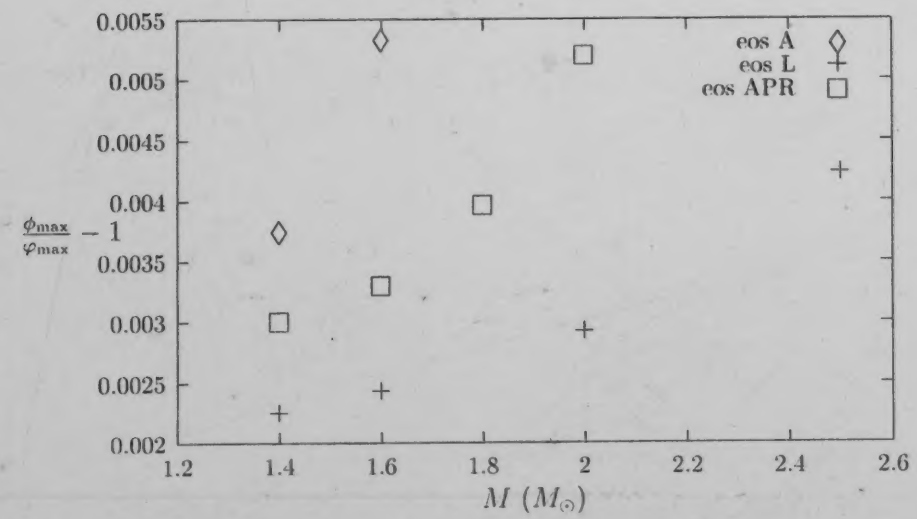

Figure 4.11: The fractional difference between $\phi_{\rm max}$ and $\varphi_{\rm max}$ for the calculated spherical neutron star models.

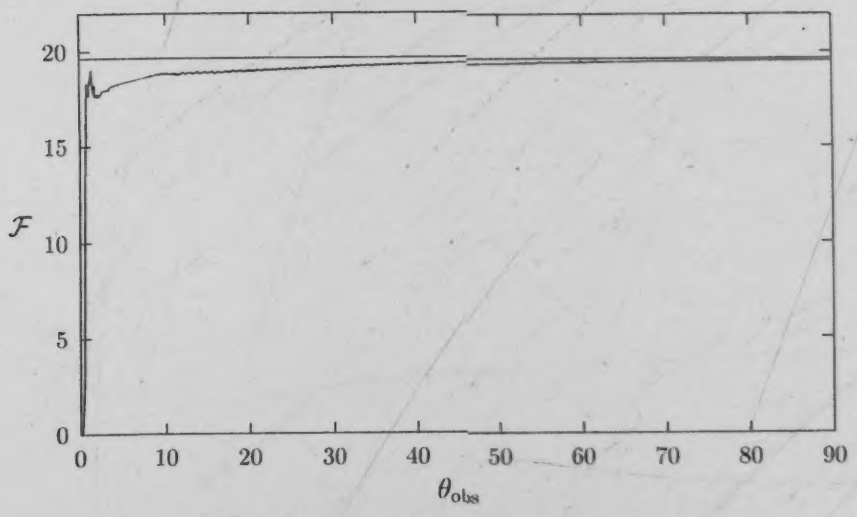

Figure 4.12: The calculated flux from a non-rotating star of eos A and mass $1.4M_\odot$ for observers at various latitudes. The constant line is $\mathcal{F}_{\rm sph}$, the expected spherical limit of the flux.

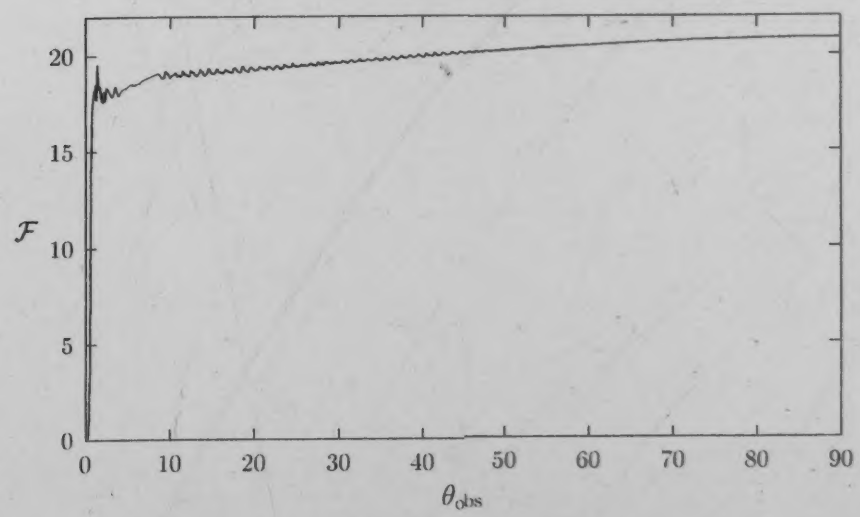

Figure 4.13: The flux from a star with eos A and mass $1.4M_\odot$ rotating with a frequency of 600 Hz for observers at different latitudes as calculated by our algorithms. This figure is meant as an indication of the current shortcomings of the code. As with figure 4.12, the vanishing of the flux at the pole is a non-physical numerical artifact. The plot should be most accurate for observers near the equator.

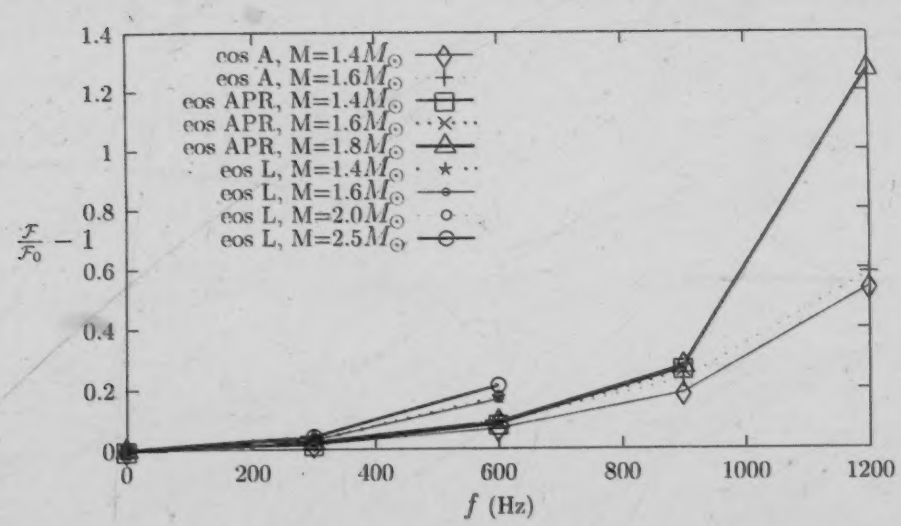

Figure 4.14: The fractional increase in measured flux by an observer in the neutron star's equatorial plane as the star's spin frequency increases.

higher than those for cos A. It is conceivable that observations of various stars could create plots similar to figure 4.14 and provide additional constraints to the neutron star's equation of state.

In flat space, the flux of a star is directly proportional to the star's surface area. So the increase in flux as a star rotates more rapidly is partially due to the increased surface area of the star as it morphs from a perfect sphere to an oblate spheriod. However, as we can see from figure 4.15, there are additional effects in curved spacetime. The surface areas of the neutron stars are determined by integrating (4.12) over the surface of the star. I would speculate that this increase in flux is due to an increase in the visible portion of the star as the star's rotation increases. Also, since the increased visible portion of the star is on the side emitting prograde photons which are Doppler blueshifted, then the net spectrum is blueshifted which increases the energy (and hence flux) of the emitted radiation received by the obeserver.

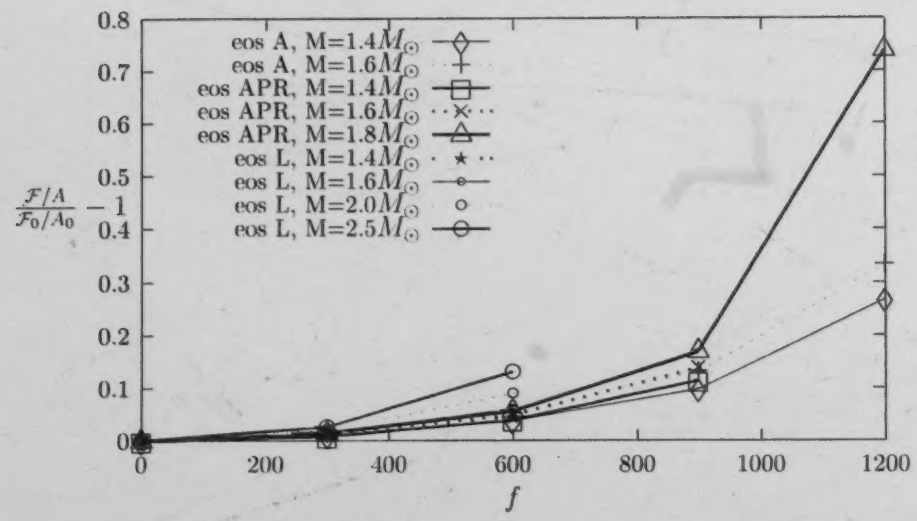

Figure 4.15: The fractional increase in measured flux per surface area of neutron stars as their spin frequencies increase.

Chapter 5

Conclusions

5.1 Summary of Completed Research

The ability of modern methods to numerically calculate tabulated space-times of rapidly rotating neutron stars to good accuracy allows for the opportunity to carry out computational calculations with these space-times. In this work, a code was developed to calculate geodesic paths within the tabulated space-time of a neutron star. The accuracy of the geodesics was verified by observing how well an independent momentum constraint is obeyed, and by comparing the computed geodesics to known exact solutions: geodesics about spherical stars, and geodesics constrained to the equatorial plane.

Once the paths of light near rapidly rotating neutron stars are known, ray-tracing methods may be implemented to calculate general relativistic effects on detected emissions from the star. Knowledge of the geodesics allows us to take the curvature of light paths and frame dragging effects into account. The total frequency shift of a photon from the stars surface to infinity was also determined, allowing our methods to also account for gravitational redshift and relativistic Doppler shifts due to the star's rotation.

The particular problem to which we applied these ideas was calculating the flux of thermal emission (approximated as blackbody) from a neutron star, as detected far from the star (by, for instance, an X-ray telescope). Photons emitted from the star's surface and propagating away from the star have initial conditions most conveniently described in an altitude-azimuth angular coordinate system. Such a system was developed within the curvature of space

around a neutron star. Our methods were tested by comparing the results for the flux of a non-rotating star to a more exact calculation. It was determined that our methods for calculating the flux from a neutron star work well if the observer is near the star's equatorial plane, but fails if the observer is near the star's pole. So we focussed on results where the observer is in the star's equatorial plane. It was found that as stars with the same gravitational mass spin with greater frequency, the flux received from them increases. This escalation in brightness cannot simply be explained by the increased surface area of the star. It is suspected that one can see further behind a rotating star and more of the observed light is blueshifted than redshifted by the Doppler effect. The increase in flux was also affected by the star's equation of state, bringing up the point that it may be possible to constrain the equation of state of dense nuclear matter by observing the thermal flux of neutron stars of known mass and frequency of rotation.

5.2 Computational Improvements Required

As successful as our programming was, there remain several shortcomings with our algorithms that need addressing. Currently, the calculation of thermal emissions from neutron stars fails if the neutron star is too near the maximum mass or maximum rotation model for the particular equation of state. For example, with eos APR, the emission of models with mass $2.0M_{\odot}$ was completed, but it gave nonsense results, and the emission of models with mass $2.2M_{\odot}$ could not be completed as it contained geodesics that crashed the Runge-Kutta solver.

The geodesic solver also needs a better way to handle geodesics that travel near the pole without originating at the pole. There are indications in the presented accuracy checks that geodesics originating near the pole of the star tend to be less accurate, or have more unusually inaccurate cases. There are other difficulties inherent with using a spherical coordinate system for our calculations. Such coordinates make calculating the flux of a star difficult to calculate for observers at the star's pole.

The blips described in section 4.6 are an inevitable consequence of computational error. Methods should be developed to recognize their occurence and be able to handle them in a consistent manner. On a similar note, stars that emit photons that will sweep an angle greater than 180^o needs to be implemented. These stars will have positions on their surfaces that can emit photons at more than 2 azimuth angles for a given altitude that will reach the observer.

5.3 Future Directions for Research

There are a few improvements that could be calculated for the purpose of determining the flux of a star. A correct account of the deviation of geodesics needs to be implemented. Also, the altitude and azimuth angles at the surface of the star are defined by a static observer. It would make more sense if they were determined in a frame co-rotating with the star.

There are many possible applications for applying ray-tracing that will be helpful to researchers having to analyze emissions from neutron stars. General relativistic effects on the emitted spectrum could be calculated, and one could investigate how one may determine the surface temperature of the star from such a spectrum. If it is possible to determine the star's temperature, then one could investigate how well the radius of the star could be estimated from the star's temperature, flux, and distance from the observer.

Broadening of spectral lines is another topic of interest. Simulations can determine the plausibility of determining stellar spin parameters from this, or the star's mass to equatorial radius ratio from the redshift of the lines.

In the future, scientists will want to use more realistic emission spectra than blackbody. Together, observations and simulations can provide strong constraints on the emitted thermal spectrum of neutron stars. Effects such as hotspots can also be considered with these methods.

Bibliography

[1] A. Akmal, V. Pandharipande, and D. Ravenhall. Equation of state of nucleon matter and neutron star structure. *Physical Review C*, 58(3):1804–1828, 1998.

[2] M. Alcubierre, S. Brandt, B. Brügmann, D. Holz, E. Seidel, R. Takahashi, and J. Thornburg. Symmetry without symmetry: Numerical simulation of axisymmetric systems using cartesian grids. *International Journal of Modern Physics D*, 10(3):273–289, 2001.

[3] W. Arnett and R. Bowers. A microscopic interpretation of neutron star structure. *Astrophysical Journal Supplement*, 33:415, 1977.

[4] O. Barziv, L. Kaper, M. Van Kerkwijk, J. Telting, and J. Van Paradijs. The mass of the neutron star in Vela X-1. *Astronomy and Astrophysics*, 377:925–944, 2001.

[5] A. Beloborodov. Gravitational bending of light near compact objects. *The Astrophysical Journal*, 566:85–88, 2002.

[6] T. Braje, R. Romani, and K. Rauch. Light curves of rapidly rotating neutron stars. *The Astrophysical Journal*, 531:447–452, 2000.

[7] P. Byrd and M. Friedman. *Handbook of Elliptic Integrals for Engineers and Scientists*. Springer-Verlag, 2nd, rev. edition, 1971.

[8] B. Carroll and D. Ostlie. *An Introduction to Modern Astrophysics*. Addison-Wesley Publishing Company, Inc., 1996.

[9] B. Carter. Global structure of the kerr family of gravitational fields. *Physical Review*, 174:1559–1571, 1968.

[10] G. Cook, S. Shapiro, and S. Teukolsky. Rapidly rotating neutron stars in general relativity: Realistic equations of state. *The Astrophysical Journal*, 424:823–845, 1994.

[11] J. Cottam, F. Paerels, and M. Mendez. Gravitationally redshifted absorption lines in the X-ray burst spectra of a neutron star. *Nature*, 420:51–54, 2002.

[12] J. Dormand. *Numerical Methods for Differential Equations: A Computational Approach*. CRC Press, 1996.

[13] J. Friedman and J. Ipser. Rapidly rotating relativistic stars. *Philosophical Transactions of the Royal Society of London A*, 340:391–422, 1992.

[14] J. Friedman, L. Parker, and J. Ipser. Rapidly rotating neutron star models. *The Astrophysical Journal*, 304:115–139, 1986. Erratum in ApJ, 351:705, 1986.

[15] C. Ftaclas, M. Kearney, and K. Pechenick. Hot spots on neutron stars. II. The observer's sky. *The Astrophysical Journal*, 300:203–208, 1986.

[16] N. Glendenning. *Compact Stars: Nuclear Physics, Particle Physics, and General Relativity*. Springer-Verlag, second edition, 2000.

[17] H. Komatsu, Y. Eriguchi, and I. Hachisu. Rapidly rotating general relativistic stars–I. Numerical method and its application to uniformly rotating polytropes. *Monthly Notices of the Royal Astronomical Society*, 237:355–379, 1989.

[18] H. Marshall. Chandra results on lines from bursters. Talk presented at the workshop Neutron Stars on Fire, Institute for Advanced Study, http://www.sns.ias.edu/~burst/Talks/marshall.pdf, May 2003.

[19] J. Matese and D. Whitmire. Effect of strong gravity on the optical appearance of rapidly fluctuating astronomical sources. *The Astrophysical Journal*, 226:501–507, 1978.

[20] C. Misner, K. Thorne, and J. Wheeler. *Gravitation.* W H Freeman & Co., 1973.

[21] H.-P. Nollert, H. Ruder, H. Herold, and U. Kraus. The relativistic "looks" of a neutron star. *Astronomy and Astrophysics*, 208:153–156, 1989.

[22] J. Orosz and E. Kuulkers. The optical light curves of Cygnus X-2 (V1341 Cyg) and the mass of its neutron star. *Monthly Notices of the Royal Astronomical Society*, 305:132–142, 1999.

[23] F. Özel and D. Psaltis. Spectral lines from rotating neutron stars. *The Astrophysical Journal*, 582:L31–L34, 2003.

[24] V. Pandharipande. Dense neutron matter with realistic interactions. *Nuclear Physics A*, 174:641–656, 1971.

[25] V. Pandharipande and R. Smith. Nuclear matter calculations with mean scalar fields. *Physics Letters B*, 59:15–18, 1975.

[26] K. Pechenick, C. Ftaclas, and J. Cohen. Hot spots on neutron stars: The near-field gravitational lens. *The Astrophysical Journal*, 274:846–857, 1983.

[27] K. Rauch and R. Blandford. Optical caustics in a kerr spacetime and the origin of rapid X-ray variability in active galactic nuclei. *The Astrophysical Journal*, 421:46–68, 1994.

[28] R. Rutledge, L. Bildsten, E. Brown, G. Pavlov, and V. Zavlin. Quiescent thermal emission from the neutron star in Aquila X-1. *The Astrophysical Journal*, 559(2):1054–1059, 2001.

[29] B. Schutz. *A First Course in General Relativity.* Cambridge University Press, 1985.

[30] S. Shapiro and S. Teukolsky. *Black Holes, White Dwarfs, and Neutron Stars: The Physics of Compact Objects.* John Wiley & Sons, 1983.

[31] F. Shu. *Radiation*, volume 1 of *The Physics of Astrophysics*. University Science Books, 1991.

[32] N. Stergioulas and J. Friedman. Comparing models of rapidly rotating relativistic stars constructed by two numerical methods. *The Astrophysical Journal*, 444:306–311, 1995. The rns code is publicly available at http://www.gravity.phys.uwm.edu/rns/.

[33] S. Weinberg. *Gravitation and Cosmology: Principles and Applications of the General Theory of Relativity*. John Wiley & Sons, 1972.

Appendix

The purpose of this appendix is to calculate the distance from the plane of motion of a photon propagating outside a spherical star. Given the initial position of the geodesic (stated by the polar coordinate μ) and the initial direction of propagation with altitude h and azimuth angle A, we can determine the plane of motion of the photon. If $\mathbf{r}_o$ is the initial position of the photon and $\dot{\mathbf{r}}_o$ is the initial λ-derivative, then all the points $\mathbf{r}$ in the photon's plane of motion satisfy $(\mathbf{r}_o \times \dot{\mathbf{r}}_o) \cdot \mathbf{r} = 0$. In terms of Cartesian coordinates

$$\begin{aligned} x &= r\sqrt{1-\mu^2}\cos\phi \\ y &= r\sqrt{1-\mu^2}\sin\phi \\ z &= r\mu \end{aligned}$$

the plane equation is $a_1 x + a_2 y + a_3 z = 0$ where a_1, a_2, and a_3 are constants. It follows that the initial position is given by

$$\mathbf{r}_o = r_o\sqrt{1-\mu_o^2}\hat{\mathbf{x}} + r_o\mu_o\hat{\mathbf{z}}.$$

Taking the λ-derivatives of the Cartesian coordinates and evaluating them at the initial geodesic position, we have

$$\begin{aligned} \dot{x}_o &= \sqrt{1-\mu_o^2}\dot{r}_o - \frac{r_o\mu_o}{\sqrt{1-\mu_o^2}}\dot{\mu}_o \\ \dot{y}_o &= r_o\sqrt{1-\mu_o^2}\dot{\phi}_o \\ \dot{z}_o &= \mu_o\dot{r}_o + r_o\dot{\mu}_o \end{aligned}$$

and we write the velocity components in terms of the altitude and azimuth angles using the results of section 3.4.5:

$$\begin{aligned}
\dot{x}_o &= \epsilon e^{-\alpha_o-(\gamma_o+\rho_o)/2}\frac{\sqrt{1-\mu_o^2}D-\mu_o}{\sqrt{1+D^2}}\sqrt{\frac{1-\cos^2 h\sin^2 A}{1-v_o^2}} \\
\dot{y}_o &= e^{-\gamma_o}\cos h\sin A \\
\dot{z}_o &= \epsilon e^{-\alpha_o-(\gamma_o+\rho_o)/2}\frac{\mu_o D+\sqrt{1-\mu_o^2}}{\sqrt{1+D^2}}\sqrt{\frac{1-\cos^2 h\sin^2 A}{1-v_o^2}}.
\end{aligned}$$

So the constants of the plane equation are

$$\begin{aligned}
a_1 &= y_o\dot{z}_o - z_o\dot{y}_o = -e^{-\gamma_o}r_o\mu_o\cos h\sin A \\
a_2 &= z_o\dot{x}_o - x_o\dot{z}_o = -e^{-\gamma_o}\frac{\epsilon r_o}{\sqrt{1+D^2}}\sqrt{\frac{1-\cos^2 h\sin^2 A}{1-v_o^2}} \\
a_3 &= x_o\dot{y}_o - y_o\dot{x}_o = e^{-\gamma_o}r_o\sqrt{1-\mu_o^2}\cos h\sin A.
\end{aligned}$$

Substitute this result into the plane equation written in spherical coordinates, and divide the result by $-rr_o e^{-\gamma_o}$ to get

$$\begin{aligned}
0 &= \epsilon e^{-\alpha_o+(\gamma_o-\rho_o)/2}\sqrt{\frac{1-\cos^2 h\sin^2 A}{(1+D^2)(1-v_o^2)}}\sqrt{1-\mu^2}\sin\phi \\
&\quad + \cos h\sin A(\mu_o\sqrt{1-\mu^2}\cos\phi - \sqrt{1-\mu_o^2}\mu),
\end{aligned}$$

the plane of motion for the geodesic.

Now given a plane $a_1x + a_2y + a_3z = 0$ and position in space $\mathbf{r}_f$, we want to determine the minimum distance between the plane and the point. Let $\mathbf{r}_p$ be a point on the plane. The distance betweent the two points is

$$\begin{aligned}
\ell &= |\mathbf{r}_f - \mathbf{r}_p| = \sqrt{(x_f-x_p)^2+(y_f-y_p)^2+(z_f-z_p)^2} \\
&= \sqrt{(x_f-x_p)^2+(y_f-y_p)^2+\left(z_f+\frac{a_1}{a_3}x_p+\frac{a_2}{a_3}y_p\right)^2}.
\end{aligned}$$

To minimize ℓ, set its partial derivatives with respect to x_p and y_p,

$$\begin{aligned}
\frac{\partial\ell}{\partial x_p} &= \frac{1}{\ell}\left[\left(1+\frac{a_1^2}{a_3^2}\right)x_p+\frac{a_1a_2}{a_3^2}y_p - x_f+\frac{a_1}{a_3}z_f\right] \\
\frac{\partial\ell}{\partial y_p} &= \frac{1}{\ell}\left[\left(1+\frac{a_2^2}{a_3^2}\right)y_p+\frac{a_1a_2}{a_3^2}x_p - y_f+\frac{a_2}{a_3}z_f\right],
\end{aligned}$$

simultaneously to zero and solve for x_p and y_p. Then use the plane equation to determine z_p. The results are

$$\begin{aligned} x_p &= \frac{(a_2^2+a_3^2)x_f - a_1a_2y_f - a_1a_3z_f}{a_1^2+a_2^2+a_3^2} \\ y_p &= \frac{-a_1a_2x_f + (a_1^2+a_3^2)y_f - a_2a_3z_f}{a_1^2+a_2^2+a_3^2} \\ z_p &= \frac{-a_1a_3x_f - a_2a_3y_f + (a_1^2+a_2^2)z_f}{a_1^2+a_2^2+a_3^2}. \end{aligned}$$

It then turns out that the distance between the point and the plane is

$$\ell = \frac{|a_1x_f + a_2y_f + a_3z_f|}{\sqrt{a_1^2+a_2^2+a_3^2}}.$$

Substituting the constants for the geodesic's plane of motion, the distance between the point $\mathbf{r}_f$ and the plane of motion is

$$\ell = r_f \frac{\left|C_1\left(\mu_o\sqrt{1-\mu_f^2}\cos\phi_f - \sqrt{1-\mu_o^2}\mu_f\right) + C_2\sqrt{1-\mu_f^2}\sin\phi_f\right|}{\sqrt{C_1^2+C_2^2}}$$

where

$$\begin{aligned} C_1 &= e^{(\rho_o-\gamma_o)/2}\cos h\sin A \\ C_2 &= e^{-\alpha_o}\epsilon\sqrt{\frac{1-\cos^2 h\sin^2 A}{1+D^2}}. \end{aligned}$$